

THE SIMPLE SURVEY: OBSERVATIONS, REDUCTION, AND CATALOG

M. DAMEN¹, I. LABBÉ², P. G. VAN DOKKUM³, M. FRANK¹, E. N. TAYLOR⁴, W. N. BRANDT⁵, M. DICKINSON⁶, E. GAWISER⁷, G. D. ILLINGWORTH⁸, M. KRIEK⁹, D. MARCHESINI¹⁰, A. MUZZIN³, C. PAPOVICH¹¹, H.-W. RIX¹²

Accepted for publication in the Astrophysical Journal

ABSTRACT

We present the *Spitzer* IRAC/MUSYC Public Legacy Survey in the Extended CDF-South (SIMPLE), which consists of deep IRAC observations covering the $\sim 1,600$ arcmin² area surrounding GOODS-S. The limiting magnitudes of the SIMPLE IRAC mosaics typically are 23.8, 23.6, 21.9, and 21.7, at 3.6 μ m, 4.5 μ m, 5.8 μ m, and 8.0 μ m, respectively (5- σ total point source magnitudes in AB). The SIMPLE IRAC images are combined with the 10' \times 15' GOODS IRAC mosaics in the center. We give detailed descriptions of the observations, data reduction, and properties of the final images, as well as the detection and photometry methods used to build a catalog. Using published optical and near-infrared data from the Multiwavelength Survey by Yale-Chile (MUSYC), we construct an IRAC-selected catalog, containing photometry in *UBVRIz'JHK*, [3.6 μ m], [4.5 μ m], [5.8 μ m], and [8.0 μ m]. The catalog contains 43,782 sources with S/N > 5 at 3.6 μ m, 19,993 of which have 13-band photometry. We compare this catalog to the publicly available MUSYC and FIREWORKS catalogs and discuss the differences. Using a high signal-to-noise sub-sample of 3,391 sources with $([3.6]+[4.5])/2 < 21.2$, we investigate the star formation rate history of massive galaxies out to $z \sim 1.8$. We find that at $z \sim 1.8$ at least $30\% \pm 7\%$ of the most massive galaxies ($M_* > 10^{11} M_\odot$) are passively evolving, in agreement with earlier results from surveys covering less area.

Subject headings: catalogs – galaxies: evolution – galaxies: observations – galaxies: photometry – infrared: galaxies

1. INTRODUCTION

Our understanding of galaxy formation and evolution has dramatically increased through the rise of large and deep galaxy surveys that have opened up the high-redshift universe for research. The best studied high-redshift galaxies are arguably the Lyman break galaxies (LBGs) that can be identified by their rest-frame UV colors (Steidel et al. 1996; 1999). Although much has been learned from studying their properties, LBGs are not representative for all high-redshift galaxy populations. Since they are based on selection in the rest-frame UV,

optical surveys of high-redshift galaxies are heavily affected by dust obscuration and are not sensitive to old stellar populations. The rest-frame optical is less influenced by the contribution from young stars and dust and provides a more reliable means of tracing the bulk of the stellar mass at high redshift. For instance, near-infrared observations have uncovered a significant population of massive, red galaxies, particularly at high redshift (Elston, Rieke & Rieke 1988, Spinrad et al. 1997, Barger et al. 1999, Daddi et al. 2000, Franx et al. 2003, Labbé et al. 2003, Cimatti et al. 2004, van Dokkum et al. 2006).

With the arrival of the *Spitzer Space Telescope* and its Infrared Array Camera (IRAC; Fazio et al. 2004), constructing large surveys to study high-redshift galaxies has become even more attainable, since the IRAC wavelengths provide coverage of the rest-frame optical bands out to higher redshifts. Using deep IRAC observations at 4.5 μ m it is possible to trace the rest-frame *I*-band out to a redshift $z \sim 4$.

The massive, red galaxies found at high redshift are important test-beds for models of galaxy formation and evolution. To be able to place constraints on the models we need a clear picture of the evolution and star formation history of these massive galaxies. This requires large, statistically powerful samples, or in other words, surveys that extend over a great area and depth. It is also critical to do these observations in areas that already have been observed at many wavelengths and ideally in areas that are accessible to future telescopes such as ALMA. The 30' \times 30' Extended Chandra Deep Field South (E-CDFS) is perfect in this sense as it is one of the most extensively observed fields available.

damen@strw.leidenuniv.nl

¹ Leiden Observatory, Leiden University, PO Box 9513, 2300 RA Leiden, The Netherlands

² Carnegie Observatories, 813 Santa Barbara Street, Pasadena, CA 91101, USA; Hubble Fellow

³ Department of Astronomy, Yale University, New Haven, CT, 06520, USA

⁴ School of Physics, The University of Melbourne, Parkville, 3010, Australia

⁵ Department of Astronomy and Astrophysics, The Pennsylvania State University, University Park, PA 16802, USA

⁶ NAOJ, 950 N. Cherry Avenue, Tucson, AZ 85719, USA

⁷ Department of Physics and Astronomy, Rutgers University, Piscataway, NJ 08854, USA

⁸ UCO/Lick Observatory, University of California, Santa Cruz, CA 95064, USA

⁹ Harvard-Smithsonian Center for Astrophysics, 60 Garden Street, Cambridge, MA 02138

¹⁰ Department of Physics and Astronomy, Tufts University, Medford, MA 02155, USA

¹¹ George P. and Cynthia Woods Mitchell Institute for Fundamental Physics and Astronomy, Department of Physics and Astronomy, Texas A&M University, 4242 TAMU, College Station, TX 77843, USA

¹² Max-Planck-Institut für Astronomie, Königstuhl 17, D-69117 Heidelberg, Germany

TABLE 1
N- σ LIMITING DEPTHS (TOTAL AB MAGNITUDE)

Program	area	channel	depth (AB mag)	S/N	integration time
GOODS-S	138 arcmin ²	3.6 μm	26.15	3	23 hr
		4.5 μm	25.66		
		5.8 μm	23.79		
		8.0 μm	23.70		
SIMPLE	1,600 arcmin ²	3.6 μm	23.86	5	0.9-2.5 hr
		4.5 μm	23.69		
		5.8 μm	21.95		
		8.0 μm	21.84		
S-COSMOS	2 deg ²	3.6 μm	24.0	5	1200 s
		4.5 μm	23.3		
		5.8 μm	21.3		
		8.0 μm	21.0		
SWIRE	60 deg ²	3.6 μm	21.4	10	120-480 s
		4.5 μm	21.4	5	
		5.8 μm	19.8		
		8.0 μm	19.9		

There is a large set of ground-based data providing *UBVRIZ'JHK* imaging (MUSYC (Gawiser et al. 2006, Quadri et al. 2007, Taylor et al. 2009b), COMBO-17 (Wolf et al. 2004), LCIRS, (McCarthy et al. 2001)), radio coverage (Miller et al. 2008), and spectroscopy (e.g., GOODS (VIMOS: Popesso et al. 2009, FORS2: Szokoly et al. 2004, Vanzella et al. 2008), MUSYC (Treister et al. 2009a), K20 (Cimatti et al. 2002), VVDS (le Fèvre et al. 2004)). The area has been targeted intensely from space too. There is HST ACS imaging from GEMS (Rix et al. 2004), observations from CHANDRA (Lehmer et al. 2005, Luo et al. 2008), XMM (PI: J. Bergeron), GALEX (Martin et al. 2005), and ultra deep multiwavelength coverage from the Great Observatories Origins Deep Survey (GOODS, Dickinson et al. 2003) in the central $10' \times 15'$. The rich multiwavelength coverage includes also deep 24, 70, and 160 μm observations from the Far-Infrared Deep Extragalactic Legacy Survey (FIDEL).

In this context, we initiated *Spitzer's* IRAC + MUSYC Public Legacy of the E-CDFS (SIMPLE), which aims to provide deep, public IRAC imaging of a 1,600 arcmin² area on the sky. In this paper, we present the full IRAC data set, with an IRAC-selected multicolor catalog of sources with 13-band optical-to-infrared photometry (covering 0.3-8.0 μm). The optical to near-infrared (NIR) data come from the Multiwavelength Survey by Yale-Chile (MUSYC; Taylor et al. 2009), which are publicly available¹³. We also included the 24 μm data from FIDEL, which reaches a depth of $\sim 40\mu\text{Jy}$.

In addition to the study of massive galaxies, the SIMPLE survey can be used to analyze properties of active galactic nuclei (AGNs). Luminous optically unobscured AGN can be selected based on their IRAC colors (Lacy et al. 2005, Stern et al. 2005). In the case of dust-obscured AGNs, the energy absorbed at optical to X-ray wavelengths is later re-emitted in the mid-IR. AGNs should therefore by very bright mid-IR sources (e.g., Daddi et al. 2007, Alexander et al. 2008, Donley et al. 2008). The SIMPLE survey has proved valuable

in this context (Cardamone et al. 2008, Treister et al. 2009a, 2009b) and the full photometric data set in the E-CDFS can provide strong constraints on the redshifts, masses, and stellar populations of the host galaxies. One example is the study by Luo et al. (2010), who use the SIMPLE survey (among other data sets) to improve photometric redshifts of X-ray AGN hosts. Their work also shows the value of the SIMPLE survey regarding the identification of X-ray selected AGNs. These sources can be very difficult to identify at faint counterpart magnitudes. Luo et al. (2010) quantify a counterpart recovery rate and found that the SIMPLE 3.6 μm data score high in that respect (see their Table 1). To conclude the list of SIMPLE applications, IRAC observations have been useful in investigating the stellar populations of Ly α -emitting galaxies (Lai et al. 2008). Here, we focus on the observations, data reduction processes, and the construction of the catalog. This paper is structured as follows. In Section 2, we describe the observations with IRAC. Section 3 explains the reduction processes and the combined IRAC mosaics. The ancillary data from the MUSYC and FIDEL surveys that we use are described in Section 4. Source detection and photometry are discussed in Section 5. In Section 6.1, we examine our photometric redshifts by comparing them to a compilation of spectroscopic redshifts. The catalog parameters are listed and explained in Section 7 and Section 8 describes the comparison of the SIMPLE catalog with two other catalogs of the (E-)CDFS. In a recent paper (Damen et al. 2009a), we used the SIMPLE catalog to study the evolution of star formation in massive galaxies. Those results were based on a preliminary version of the catalog and we update the conclusions in Section 9. Finally, Section 10 provides a summary of the paper.

Throughout the paper we assume a Λ CDM cosmology with $\Omega_m = 0.3$, $\Omega_\Lambda = 0.7$, and $H_0 = 70 \text{ km s}^{-1} \text{ Mpc}^{-1}$. All magnitudes are given in the AB photometric system. We denote magnitudes from the four *Spitzer* IRAC channels as [3.6], [4.5], [5.8], and [8.0], respectively. Stellar masses are determined assuming a Kroupa (2001) initial mass function (IMF).

¹³ <http://www.astro.yale.edu/MUSYC>

2. OBSERVATIONS

The SIMPLE IRAC Legacy survey consists of deep observations with IRAC (Fazio et al. 2004) covering the ~ 1600 arcmin² area centered on the GOODS-IRAC imaging (Dickinson et al. 2003) of the CDFS (Giacconi et al. 2002). The survey is complementary in area and depth to other legacy programs, such as GOODS-IRAC (138 arcmin², 1380 minutes (Dickinson et al. 2003)), S-COSMOS (2 deg², 20 minutes (Sanders et al. 2007)), the Spitzer Wide-Area InfraRed Extragalactic Survey (SWIRE; 60 deg², 2-8 minutes (Lonsdale et al. 2003)), the Spitzer Ultra Deep Survey (SpUDS; 0.8 deg², ~ 120 minutes (PI: J. Dunlop)), and the Spitzer Deep, Wide-Field Survey (SDFWS; 10 deg², 6 minutes, including the Irac Shallow Survey (ISS) (Ashby et al. 2009)) (see Table 1 for more details). The goal of the SIMPLE survey was to map a large area around the CDFS, with an optimum overlap with existing surveys such as the GEMS project (Galaxy Evolution from Morphology and SEDs), COMBO-17, and MUSYC. The area of the CDFS appears as a hole in the center of the mosaic. The central coordinates of the field are: $\alpha = 3^h 32^m 29.^s 460$, $\delta = -27^\circ 48' 18''.32$, J2000). Figure 1 illustrates the field of the main surveys of the E-CDFS: GOODS (IRAC and ACS), GEMS, COMBO-17, MUSYC, and SIMPLE. The SIMPLE IRAC Legacy program was observed under program number GO 20708 (PI: van Dokkum). The complete set of observations consists of 36 pointings. On each pointing the mapping mode was used to observe a 2×3 rectangular grid, with each grid position receiving 30 minutes integration, for a total of 3 hr per pointing. The grand total exposure time was ~ 105 hr. The 2×3 map grids partially overlap, leading to an average exposure time on the sky of ~ 1.5 hr. The observations were split in two epochs, approximately 6 months apart. The observations were split in two epochs, approximately 6 months apart. The telescope orientation was rotated $\sim 170^\circ$ between the two epochs and this ensured that the area of the E-CDFS was fully covered in all four IRAC bands. This is illustrated in Fig. 2, which shows the exposure coverage of channel 1 (3.6 μm ; left) and channel 2 (4.5 μm ; right). Solid lines indicate the outline of all observations from the first epoch, dashed lines those of the second. IRAC observes in pairs: 3.6 and 5.8 μm simultaneously on one field and 4.5 and 8.0 μm on an adjacent field. Due to this construction and the telescope rotation between the two epochs, the full area was covered by all bands after completion of the observations. A summary of the observations is given in Table 2. The raw data and the observational details can be obtained from the *Spitzer* Archive with the Leopard software package¹⁴.

3. DATA REDUCTION

The reduction of the IRAC data was carried out using the Basic Calibrated Data (BCD) generated by the *Spitzer* Science Center (SSC) pipeline and a custom-made pipeline that post-processes and mosaicks the BCD frames. The reduction includes the following

TABLE 2
OBSERVATIONS

<i>Spitzer</i> program ID	20708
Target name	E-CDFS
R.A. (J2000)	$3^h 32^m 29.^s 46$
Decl (J2000)	$-27^\circ 48' 18''.32$
Start date ep1	2005 Aug 19 (week 91)
End date ep1	2005 Aug 23 (week 91)
Start date ep2	2006 Feb 06 (week 115)
End date ep2	2006 Feb 11 (week 116)

steps:

- SSC pipeline processing (Section3.1)
- Artifact correction (Section3.2.1)
- Cosmic ray rejection (Section3.2.2)
- Astrometry (Section3.2.3)
- Image combination and mosaicking (Section3.3)
- Flux calibration (Section3.4)
- Exposure time and RMS maps (Section3.5.1)
- Flag maps (Section3.5.2)

3.1. SSC Pipeline Processing

The starting point for the reduction are the BCD frames produced by SSC pipeline. The epoch 1 observations were processed by BCD pipeline version S12.4.0. The epoch 2 data were processed using pipeline version S13.2.0. The main differences between these two versions are related to pointing refinement, muxstriping, and flux conversion. These issues are all addressed separately in our own reduction pipeline, and hence these updates have no effect on the end product. An additional enhancement of S13.2.0 is the introduction of a super sky flat image, based on the first two years of IRAC of flat-field data. This has only a small effect on the data of at most 0.5%. The most significant steps of the SSC IRAC reduction pipeline are dark subtraction, detector linearization, flat-fielding, and cosmic ray detection. The data are calibrated in units of $MJysr^{-1}$. The pipeline also identifies bad pixels, which it flags and writes to a mask image, and constructs initial masks for cosmic rays (called "brmsk").

3.2. Post-processing of the BCD Frames

We post-process the BCD frames to correct for several artifacts caused by highly exposed pixels (primarily bright stars and cosmic rays) and calibrate the astrometry. In this section, we briefly describe some of the artifacts and how we try to remove them. More detailed information can be found in the IRAC Data Handbook, Section 4¹⁵. The subsequent reduction steps are similar,

¹⁴ <http://ssc.spitzer.caltech.edu/propkit/spot/>

¹⁵ <http://ssc.spitzer.caltech.edu/irac/dh>

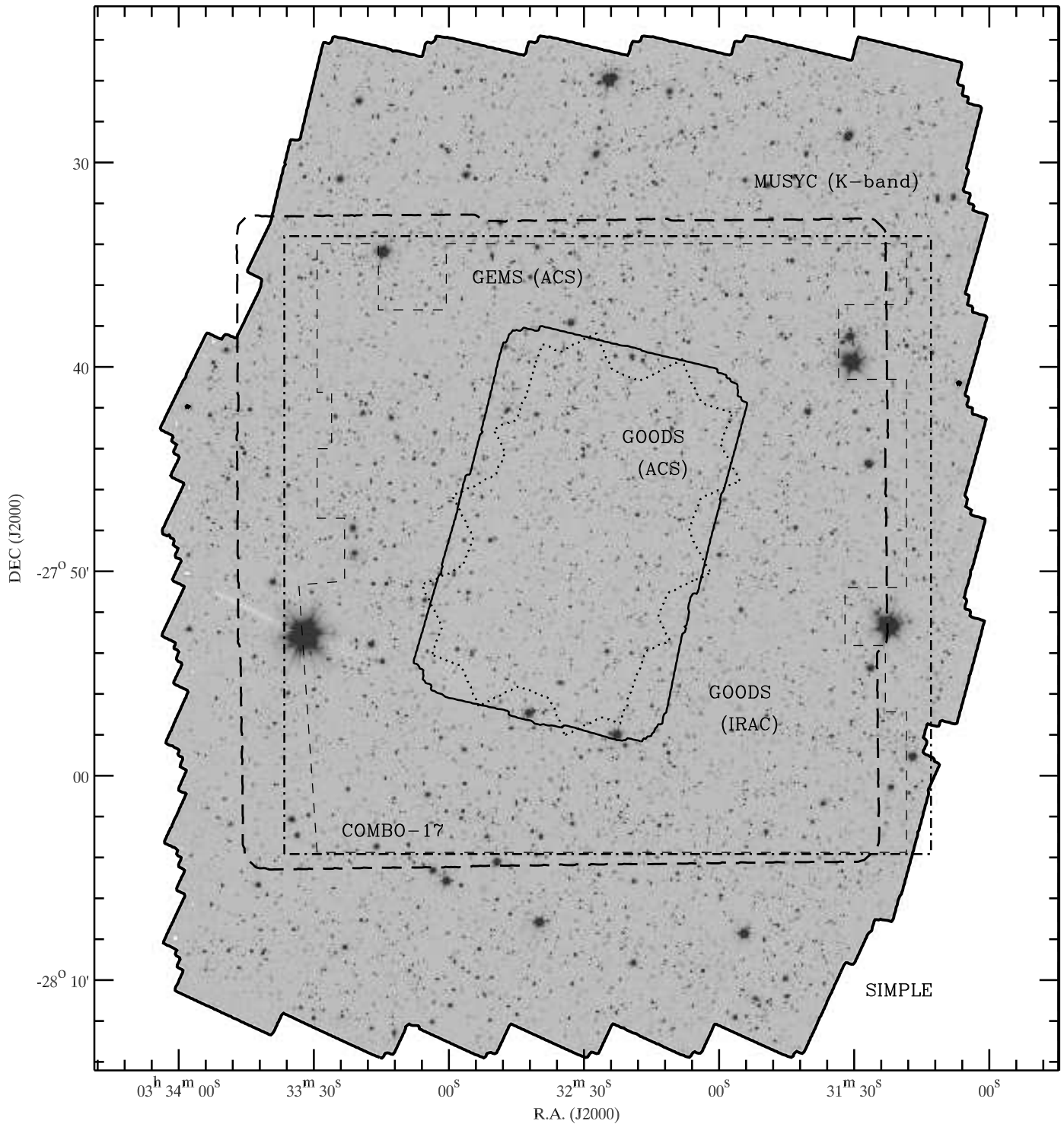


FIG. 1.— E-CDFS in the combined $3.6\ \mu\text{m} + 4.5\ \mu\text{m}$ detection image. The image is normalized by the square root of the weight map, producing a noise-equalized detection image (see Section 5.1). The thin dashed lines delineate the GEMS field, COMBO-17 is represented by the dash-dotted lines, the dotted and solid lines indicate the field of view of the GOODS ACS and IRAC observations, respectively, and the long dashed lines indicate the MUSYC field.

but not identical, to those applied by the GOODS team¹⁶.

We start with discarding the two leading short exposures of each series of observations, which can suffer from the so-called first-frame effect and cannot be calibrated correctly¹⁷.

Prior to correction for the artifacts, a median sky image is constructed based on the data taken in each series of observations. This sky image is subtracted from

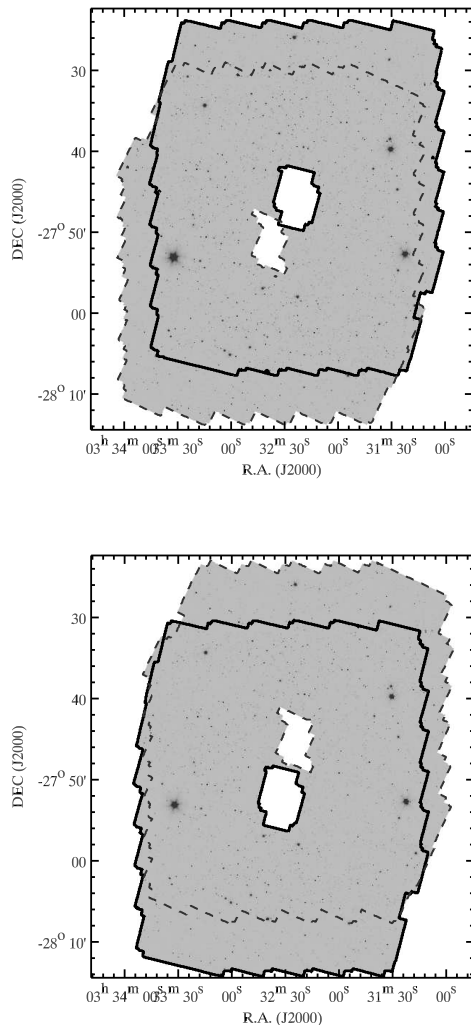


FIG. 2.— E-CDFs in channel 1 (*upper panel*) and channel 2 (*lower panel*). In both panels the data of the first epoch are indicated by the solid lines and those of the second epoch with dashed lines. Due to the special setup of IRAC, the full area is covered after the two epochs for all channels. Since channels 1 and 3 are observed simultaneously, the lines in the left panel also delineate the field of view of channel 3. The same is true for channels 2 and 4 in the right panel.

¹⁶ <http://ssc.spitzer.caltech.edu/legacy/goodshistory.html>

¹⁷ Due to the first-frame effect, the first frame of a series of observations will have a different bias offset than the rest of the observations in the sequence. Since the first image of each series is observed in "HDR-mode" (a very short exposure time of 0.4 s for identification of saturated sources), the second exposure might still suffer from this effect. It is recommended not to include these frames when building a mosaic.

each individual frame to remove both residual structure or gradients in the background caused by bias or flat fielding, and long-term persistence effects.

3.2.1. Detector Artifacts

One of the principal artifacts in IRAC data is column pull-down. When a bright star or cosmic ray reaches a level of $>\sim 35,000$ DN in the channel 1 and 2 arrays (3.6 and $4.5 \mu\text{m}$), the intensity of the column in which the bright object lies is affected. Since the intensity decreases throughout the column, this effect is called "column pull-down". While column pull-down is slightly different below and above the bright object and has a small slope, the effect is nearly constant in practice. We therefore correct for the effect by (1) locating the columns of $>\sim 35,000$ DN pixels (2) masking all bright sources in the frame, (3) calculating the median of the affected columns excluding any sources, and (4) subtracting the median. We favor this simple correction because its implementation is more robust than fitting, e.g., a general two-segment slope.

Besides column-pull-down, channels 1 and 2 suffer from an effect known as muxbleed, which appears as a trail of pixels with an enhanced and additive output level. When a bright source is read out, the readout multiplexers do not return to their cold state for some time, resulting in a pattern that trails bright sources on the row. Since columns are read simultaneously in groups of four, the effect repeats every fourth column. The amplitude of the effect decreases with increasing distance to the bright object, but it does not scale with its flux. It is therefore not possible to fit muxbleed by a simple function, and we choose for a very straightforward cosmetic correction. For each offending pixel ($> 30 M\text{Jysr}^{-1}$), we generate a list of pixels selecting every fourth pixel next in the row and previous in the row. Then, we median filter the pixel list with a filter width of 20 pixels and subtract the result. The data products (see Section 3.6) include a map that shows which pixels were muxbleed corrected.

This procedure removes the bulk of the muxbleed signal, but not all of it. However, the effect of a residual muxbleed signal in the final mosaic is reduced because of the rotation of the field between the two epochs. At different times, the muxbleed trail affects different pixels relative to the source position.

Bright stars, hot pixels, and particle or radiation hits can also generate a muxstripe pattern. Where muxbleed only affects pixels on the same row, the muxstripe pattern may extend over a significant part of the image, albeit to lower levels. Muxstriping appears as an extended jailbar pattern preceding and/or following the bright pixel. It is a fairly subtle effect, usually only slightly visible in individual frames around very bright stars, but it becomes easily visible in deeper combined frames. Muxstriping is caused by the increase of relaxation time of the multiplexer after a bright pixel is read out. It takes $\sim 10 \mu\text{s}$ to clock the next pixel onto an output, whereas the recovery time after the imprint of a bright pixel is of the order of tens of seconds. The muxstripe effect also repeats every fourth column and extends below each source. Each horizontal band of the image between two bright sources, contains the pattern induced by all sources above it and needs to be corrected accordingly.

We remove this effect by applying an offset in the zones

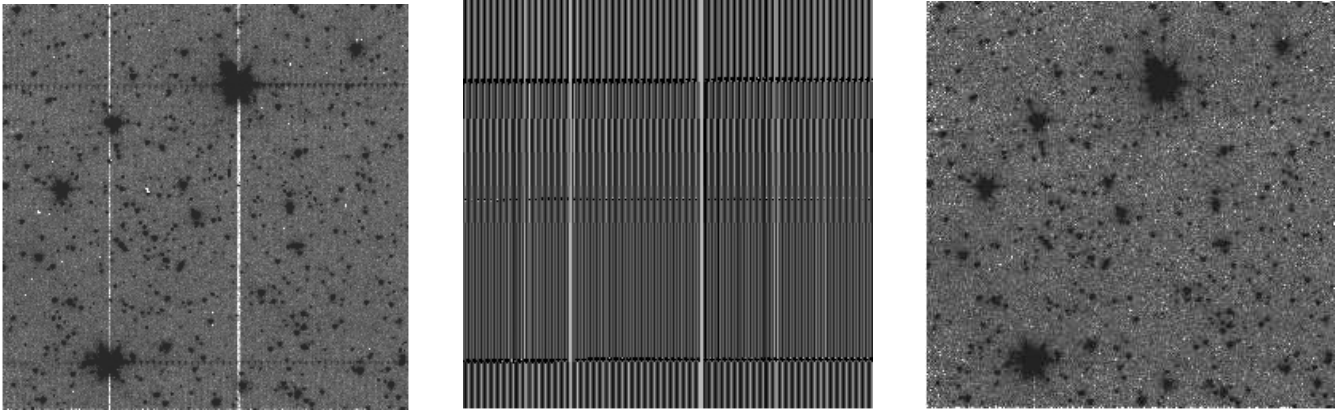


FIG. 3.— *Left* - Typical BCD frame, suffering from muxbleed (the horizontal black pattern of both sides of the bright sources), column pulldown (vertical white lines), and muxstriping (jailbar pattern that extends below each bright sources over the full width of the frame). *Center* - Correction image that is subtracted from the affected frame. *Right* - Cleaned image, after subtraction of the center frame and removal of cosmic rays. Image from Astronomical Observation Request (AOR) r15564288, channel 1, 96.4 s exposure time.

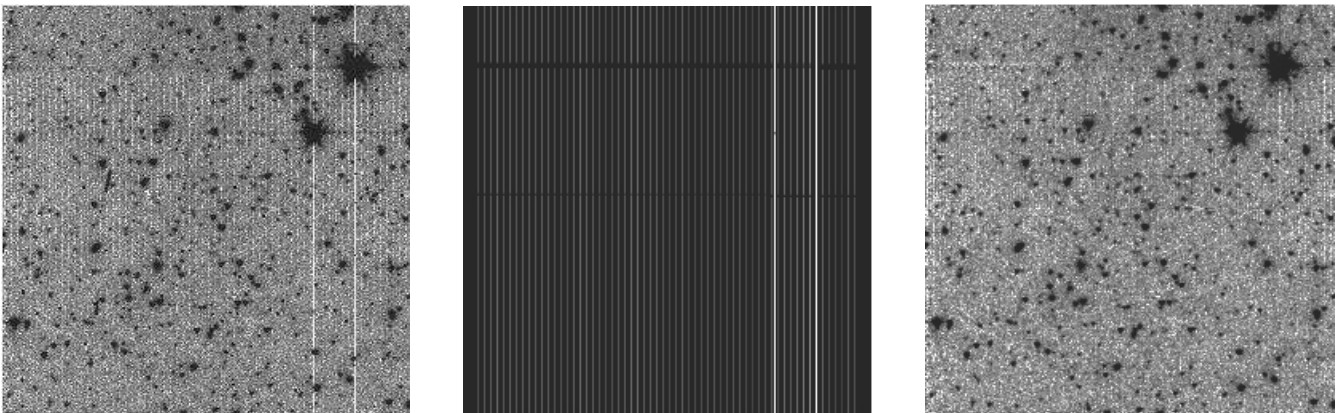


FIG. 4.— Same as Fig. 3, with more pronounced muxstriping pattern. Image from AOR r15564032, channel 1, 96.4 s exposure time.

surrounding the offending pixels using a program kindly provided by Leonidas Moustakas of the GOODS-team. In brief, this algorithm identifies the bright sources in each frame and produces a model of the corresponding muxstripe pattern, which can then be subtracted.

Figures 3 and 4 show the treatment of the artifacts just described. In the left panel, a BCD frame is affected by column pulldown, muxbleed, and muxstriping. The middle panel shows the corrections, this frame is subtracted from the affected one which results in the image on the right, a clean frame.

Finally, bright sources leave positive residuals on subsequent readouts of the array (persistence), although much of the signal subsides after 6-10 frames. We correct for persistence by creating a mask of all highly exposed pixels in a frame and then masking those pixels in the six subsequent frames. Any residual contamination through persistence will be diminished by the final combination of all exposures.

After correction for artifacts, the pipeline subtracts a constant background by (1) iteratively thresholding and masking pixels associated with sources and calculating the mode and RMS of the remaining background pixels and (2) subtracting the mode of the image.

3.2.2. Cosmic Ray Rejection

For each series of observations, a first pass registered mosaic is created from the post-processed BCD frames. For the construction of this mosaic, the BCD "brmsk"-frames are used as a first guess to mask candidate cosmic rays. The image is median combined, so it should be free of any deviant pixels.

Next, the first pass image is aligned and subtracted from each exposure. To create a cosmic ray detection image, the result is divided by the associated BCD "bunc" image, which contains estimates of the uncertainties in each pixel based on a noise model¹⁸. Pixels in this detection image are flagged as cosmic rays if they deviate more than six times the median value. Pixels adjacent to deviant pixels are also flagged using a lower threshold (factor 3.5). These flagged pixels are ignored in the analysis of the data.

3.2.3. Astrometry

The SIMPLE astrometry is calibrated to a compact-source catalog detected in a combined deep *BVR* image

¹⁸ The BCD uncertainty images are the sum of estimates of the read noise, the shot noise due to the sky and uncertainties in the dark and flat calibration files

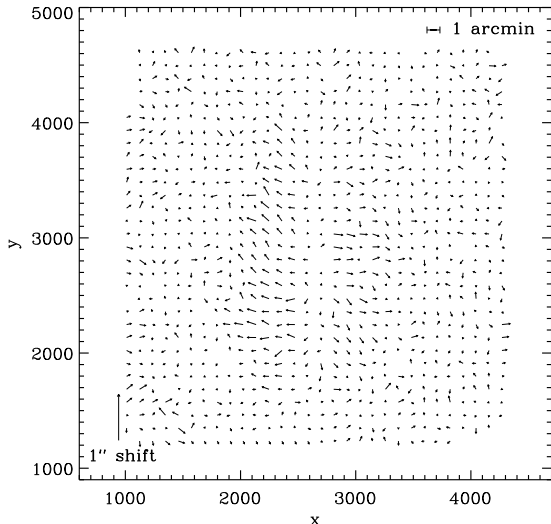


FIG. 5.— Map of residual shifts of compact sources in the $3.6 \mu\text{m}$ image with respect to a compact-source catalog detected in the deep *BVR* image. Large-scale shears, systematic variations on scales of a few arcminutes, are $0''.2$ or less.

from MUSYC¹⁹ (Gawiser et al. 2006). The calibration is done on combined frames that were taken sequentially around the same positions. The combined images are cross-matched to the *BVR* source catalog and the positions of the reference sources are measured.

The astrometric differences between the reference catalog and the SIMPLE pointings are small (up to $\sim 1''$) and can be corrected by applying a simple shift. There is no evidence for rotation, or higher order geometric distortion. We therefore apply a simple offset to the WCS CRVAL1 and CRVAL2 of the BCD frames to refine the pointing. The pointing refinement solutions determined for the 3.6 and $4.5 \mu\text{m}$ BCDs are applied to the 5.8 and $8.0 \mu\text{m}$ images, respectively, as there are generally few bright sources at 5.8 and $8.0 \mu\text{m}$ to derive them independently.

The resulting astrometry accuracy relative to the MUSYC E-CDFS *BVR* catalog is typically $\sim 0''.09$ (averaged per IRAC channel), with source-to-source $2\text{-}\sigma$ clipped RMS of $\sim 0''.12$ in channel 1/2 and $\sim 0''.14$ in channel 3/4. Large-scale shears, systematic variations on scales of a few arcminutes, are $0''.2$ or less. Figure 5 shows the residual shifts of the [$3.6 \mu\text{m}$] mosaic with respect to the MUSYC *BVR* image. The quoted astrometric uncertainties are relative to the MUSYC *BVR* catalog, but we also verified that the astrometry agrees very well ($\sim 0''.1$ level) with the “wfiRdeep” image (Gialalisco et al. 2004), which is used as a basis for the ACS GOODS astrometry.

3.3. Image Combination and Mosaicking

After individual processing, the individual BCD frames are mosaicked onto an astrometric reference grid using the refined astrometric solution in the frame headers.

¹⁹ The astrometry of the MUSYC *BVR* detection image is tied to the stellar positions of the USNO-B catalog (Monet et al. 2003)

3.3.1. Reference Grid

For the reference grid, we adopt the tangent point, pixel size, and orientation of the GOODS-IRAC images ($\alpha = 3^{\text{h}}32^{\text{m}}29.^{\text{s}}460$, $\delta = -27^{\circ}48'18''.32$, $0''.6 \text{ pixel}^{-1}$. The pixel axes are aligned with the J2000 celestial axes ²⁰.

Also following GOODS, we put the tangent point (CRVAL1,2) at a half-integer pixel position (CRPIX1,2). This ensures that images with integer pixel scale ratios (e.g., $0''.3$, $0''.6$, $1''.2$) can (in principle) be directly rebinned (block summed or replicated) into pixel alignment with one another. This puts GOODS, SIMPLE, and FIDEL (a deep $24/70 \mu\text{m}$ survey in the E-CDFS) on the same astrometric grid. The final SIMPLE mosaic extends $38' \times 48'$ (3876×4868 pixels).

3.3.2. Image Combination

For each epoch, the individual post-processed BCD frames are transformed to the reference grid using bicubic interpolation, taking into account geometric distortion of the BCD frame. Cosmic rays and bad pixels are masked and the frames are average combined without additional rejection.

Finally, the separate epoch 1 and epoch 2 mosaics are combined, weighted by their exposure times. By design, the SIMPLE E-CDFS observational strategy maps around the GOODS-S field, which leaves a hole in the combined mosaic. To facilitate the analysis, we add the GOODS-S IRAC data (DR3, mosaic version 0.3 ²⁰, to the center of the SIMPLE mosaic. We shift the GOODS-S IRAC mosaics by $\sim 0''.2$ to bring its astrometry in better agreement with SIMPLE. To ensure a seamless combination between the epoch 1, epoch 2, and GOODS-S images, we subtract an additional background from the images before combination. The background algorithm masks sources and measures the mode of the background in tiles of $1' \times 1'$. The “mode map” is then smoothed on scales of $3' \times 3'$ and subtracted from the image, resulting in extremely flat images and a zero background level on scales $> 1'$.

3.4. Flux Calibration

The SSC data are calibrated using aperture photometry in $12''$ apertures. Since ground-based IR calibrators are too bright to use for IRAC, the actual flux for each channel needs to be predicted using models (Cohen et al. 2003). The resulting calibration factors were determined by Reach et al. (2005) and are listed in the image headers and Table 3.

The epoch 1 and epoch 2 science images were scaled to a common zeropoint so that their data units agree. For convenience, we calibrate our images to the GOODS-S IRAC data (in DN s^{-1}). This is done using the original calibration factors from Table 3. The relative accuracy of the zeropoint can be estimated by minimizing the count rate differences of bright, non-saturated stars in circular apertures in regions where the images overlap. This indicates that the fluxes agree within $\sim 3\%$.

²⁰ http://data.spitzer.caltech.edu/popular/goods/20051229_enhanced

TABLE 3

channel	λ (μm)	flux conversion ^a ($\mu\text{Jy (DN s}^{-1}\text{)}^{-1}$)	zeropoint (AB)	FWHM ($''$)	Gaussian convolution ($''$)
ch1	3.6	3.922	22.416	1.97	0.84
ch2	4.5	4.808	22.195	1.93	0.93
ch3	5.8	20.833	20.603	2.06	0.80
ch4	8.0	7.042	21.781	2.23	–

NOTE. — The FWHM of the $U - K$ images is $1''.5$. To convolve those to the PSF of ch4, we use a sigma of 1.34.

^a -Listed as FLUXCONV in the image headers

3.5. Additional Data Products

3.5.1. Exposure Time and RMS Maps

The exposure time maps are created by multiplying, at each position, the number of BCD frames that were used to form the final image by the integration time of each frame. The exposure map thus reflects the exposure time

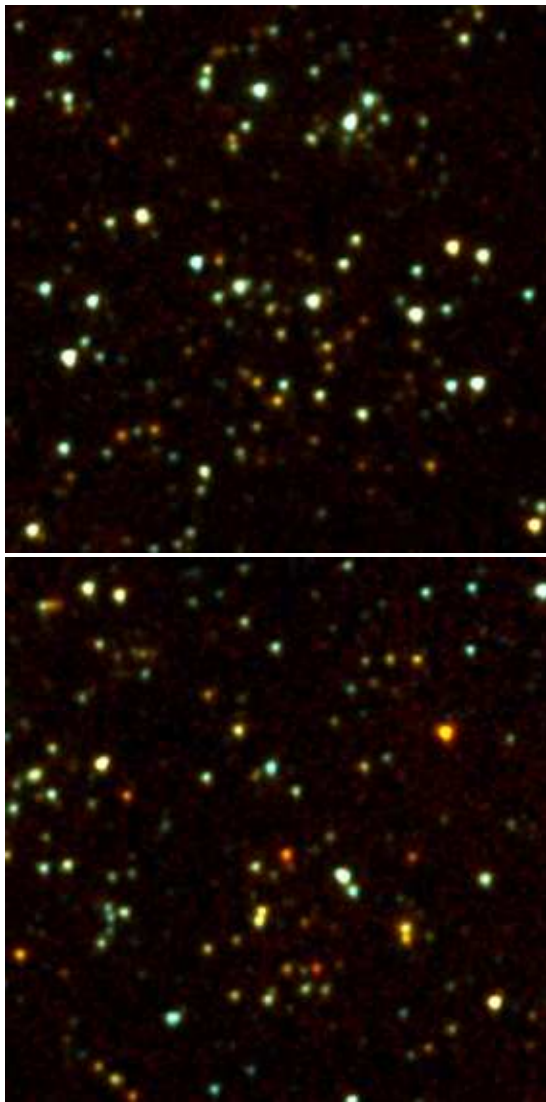


FIG. 6.— Two example zoomed-in cut-out areas showing details of the full mosaic indicated in Fig. 7: (a) left, and (b) right. The images have been enlarged 20 times. The field size is $2''.5 \times 2''.5$.

in seconds on that position of the sky, not the average exposure time per final output pixel.

The 25%, 50%, and 75% percentiles of the final exposure maps (excluding GOODS-S) are ~ 3100 , 5500 and 9100 s (0.9, 1.5 and 2.5 hr) for all channels. The corresponding area with at least that exposure time is ~ 1200 , 800, and 400 arcmin^2 , respectively. In addition, the central GOODS-S mosaic has ~ 23 hours per pointing over ~ 138 arcmin^2 .

This release also provides RMS maps. The RMS maps were created by (1) multiplying the final mosaic by the $\sqrt{(t_{exp}/\text{median}(t_{exp}))}$ (where t_{exp} is the exposure time map), to create an exposure normalized image, (2) iteratively rejecting pixels deviating $> 4.5\sigma$ and their directly neighboring pixels, (3) binning the image by a factor 4×4 , and (4) calculating the RMS statistic of the binned pixels in a moving window of 15×15 bins. The result is approximately the local RMS background variation at scales of $2''.4$ at the median exposure time, which does not suffer from correlations due to resampling. We multiply this value by $\sqrt{4}/\sqrt{(t_{exp}/\text{median}(t_{exp}))}$ to get the approximate per-pixel RMS variation at the mosaic pixel scale for other exposure times (see, e.g., Labbé et al. 2003). This RMS map does not directly reflect the contribution to the uncertainty of source confusion. The variations in the RMS due to instrumental effects are mitigated by the addition of the observed epochs under 180° different roll angles.

3.5.2. Flags

We provide a flag map, which identifies pixels corrected for muxbleed in channel 1 and channel 2. These corrections are not optimal, and when analyzing the images or constructing source catalogs, it may be useful to find pixels which may have been affected. The flag image is a bit map, i.e., an integer map that represents the sum of bit-wise added values (flag = 1 indicates a muxbleed correction in the first epoch, flag = 2 indicates a correction in the second epoch).

3.6. Final Images

The final images of SIMPLE are publicly available²¹. The data release consists of FITS images of all IRAC observations in the E-CDFS. We provide science images, exposure time maps, RMS maps, and a flag map. These images comprise combined mosaics of all data taken (both epochs), including the $10' \times 15'$ GOODS IRAC mosaics in the center. In addition, we provide combined

²¹ <http://data.spitzer.caltech.edu/popular/simple>

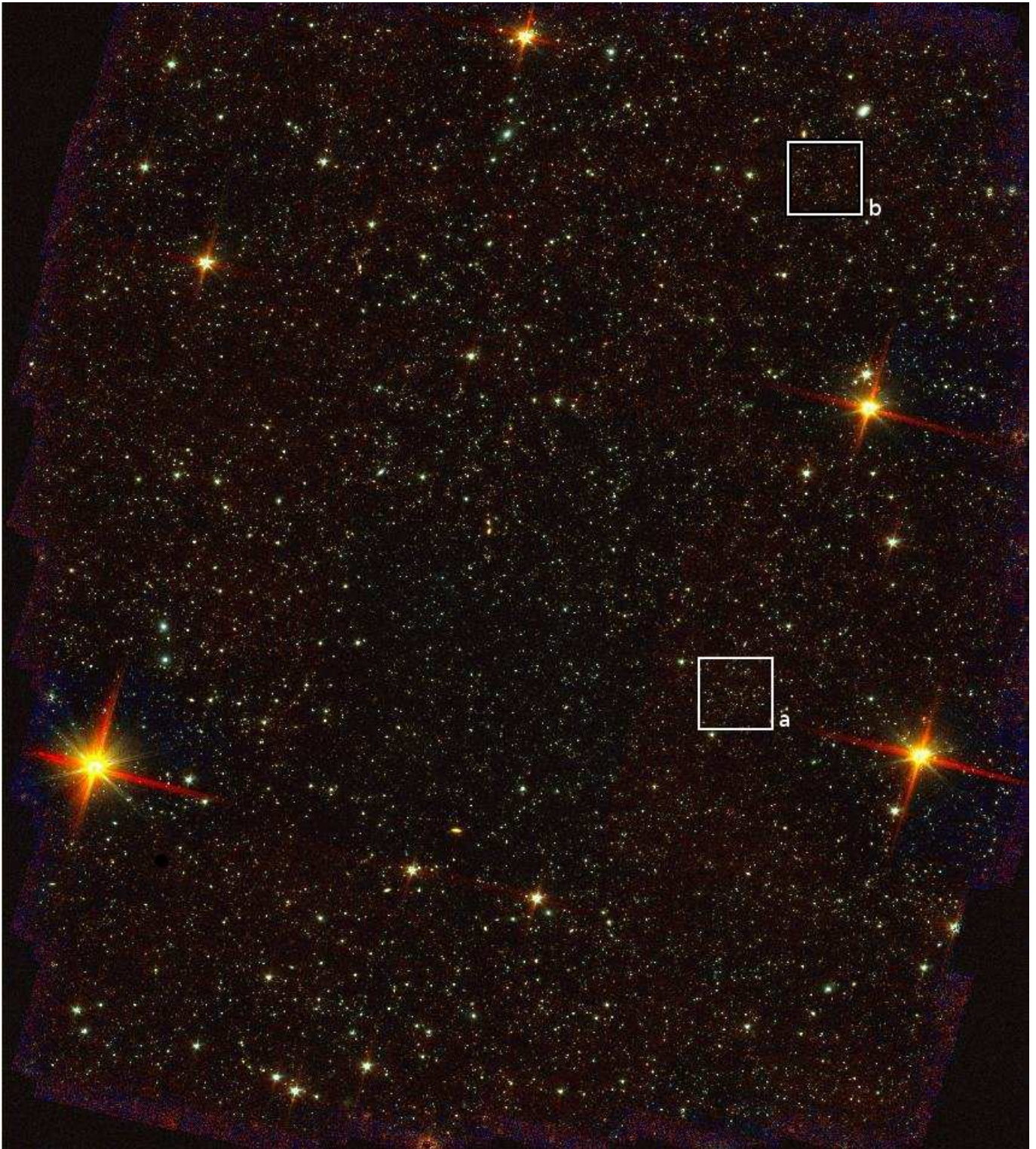


FIG. 7.— Two-color composite image of the IRAC data of the E-CDFS, based on the $3.6 \mu\text{m}$ and $5.8 \mu\text{m}$ bands. The total field size is $38' \times 48'$ and north is up. Figure 6 shows zoomed-in versions of the areas outlined in white.

mosaics and exposure maps of the data of the individual epochs (without the GOODS data), which may be useful to study the reliability and/or variability of sources. The units of the science and RMS images are DN s^{-1} , with the (GOODS) zeropoints as given in Table 3. The units of the exposure time maps are seconds. Figures 6 and 7 show the color composite image of the $3.6 \mu\text{m}$ and $5.8 \mu\text{m}$ mosaics.

4. ADDITIONAL DATA

4.1. The $U - K$ Data

To cover the optical to NIR regime, we use the *UBVRI* imaging from the COMBO-17 and ESO DPS surveys (Wolf et al. 2004 and Arnouts et al. 2001, respectively) in the re-reduced version of the GaBoDS consortium (Erben et al. 2005; Hildebrandt et al. 2006). We include the $z'JHK$ images from the Multiwavelength Survey by Yale-Chile (MUSYC, Gawiser et al. 2006), which are available online²². The final *UBVRIz'JHK* images typically have a seeing of $\sim 1''$. The images we use were PSF-matched to the image with the worst seeing (J -band, $1''.5$) by Taylor et al. (2009b). For more details on the construction of the MUSYC survey and the different data sets, we refer the reader to Taylor et al. (2009b).

4.2. The MIPS $24 \mu\text{m}$ Data

The E-CDFS was also observed extensively by the Multi-band Imaging Photometer for *Spitzer* (MIPS) as part of FIDEL (PI: M. Dickinson). The survey contains images at 24, 70, and 160 μm . We only consider the 24 μm image, due to its utility as an indicator of star formation, its sensitivity, and the fact that the source confusion at 24 μm is less severe compared to the longer wavelengths. The FIDEL 24 μm image reaches a $5\text{-}\sigma$ sensitivity ranging from 40 to 70 μJy , depending on the source position (Magnelli et al. 2009). We use the v0.2 mosaic, which was released on a scale of $1''.2 \text{ pixel}^{-1}$.

5. SOURCE DETECTION AND PHOTOMETRY

5.1. Detection

Sources are detected and extracted using the SExtractor software (Bertin & Arnouts 1996) on a detection image. The detection image is an inverse-variance weighted average of the 3.6 and $4.5 \mu\text{m}$ images. The 3.6 and $4.5 \mu\text{m}$ bands are the most sensitive IRAC bands and the combination of the two leads to a very deep detection image. To enable detection to a similar signal-to-noise limit over the entire field, we multiply the $[3.6]+[4.5]$ image by the square root of the combined exposure map. This produces a "noise-equalized" image with approximately constant signal to noise, but different depth, over the entire field. Figure 1 shows the noise-equalized detection image in the background.

Subsequently, we run SExtractor on the detection map with a $2\text{-}\sigma$ detection threshold. We choose this detection limit to be as complete as possible, at risk of severe confusion. We will discuss the matter of confusion later. In the detection process, SExtractor first convolves the detection map with a detection kernel optimized for point

sources. We use a 5×5 convolution mask of a Gaussian PSF with an FWHM of 3 pixels. Furthermore, we require a minimum of two adjacent pixels above the detection threshold to trigger a detection. The resulting catalog contains 61,233 sources, 43,782 of which have a signal-to-noise ratio (S/N) > 5 at $3.6 \mu\text{m}$.

Instead of our exposure time-detection image, we could have used the RMS map for detection. In practice, the RMS should be proportional to $1/\sqrt{(t_{exp})}$ and the choice of detection image should not significantly influence the output catalog. To test the correspondence of RMS and $1/\sqrt{(t_{exp})}$, we multiplied the RMS by the square root of the exposure time map, which results in a tight Gaussian distribution with a width of $\sigma = 0.003$. Our exposure time detection image is therefore very similar to a detection image based on an RMS map.

As an aside, we note that SExtractor's RMS map underestimates the true noise as the pixels are correlated (see, e.g., Labbé et al. 2003). If we use SExtractor's RMS map, we find $\sim 10\%$ more objects than with our method, as expected. Many of these objects are near the edges of the image; none of them have an $\text{S/N} > 5$.

5.2. Photometry

5.2.1. Image Quality and PSF Matching

In order to obtain consistent photometry in all bands, we smooth all images (except MIPS) to a common PSF, corresponding to that of the $8.0 \mu\text{m}$, which has the broadest FWHM. To determine the FWHM, we compile a list of stars with $(J - K_s) < 0.04$. We select five different areas of the E-CDFS to check whether the PSF changes over the field. This is in particular important for the IRAC bands, which have a triangular-shaped PSF. Because of the rotation between the two epochs, the final IRAC PSF is a combination of two triangular-shaped PSFs that are rotated with respect to each other. This combined PSF can vary with position in the field of view and we first need to check how large these variations are. Radial profiles of the stars are determined using the IRAF task *imexam*. We find that the variation of the mean FWHM over the whole field of view is $< 5\%$ for all IRAC bands and there is no clear trend between the mean FWHM and the position on the field for any IRAC band. We convolve all images with a Gaussian to produce similar PSFs in all bands. The mean original FWHM per band and the Gaussian sigma values used for convolution are listed in Table 3.

5.2.2. *UBVRIz'JHK + IRAC*

We run SExtractor in dual-image mode, meaning that the program determines the location of sources in the combined $[3.6]+[4.5]$ detection image, and then measures the fluxes in the smoothed science images in the exact same apertures. We perform photometry in fixed circular aperture measurements in all bands for each object, at radii of $1''.5$, $2''.0$, and $3''.0$. In addition, we use SExtractor's autoscaling apertures based on Kron (1980) radii. Following Labbé et al. (2003), we refer to these apertures as APER(1.5), APER(2.0), APER(3.0), and APER(AUTO). We use these apertures to derive both color fluxes and total fluxes (see Labbé et al. 2003). SExtractor provides a flag to identify blended sources that we include in our catalog as "flag_blended". In the

²² <http://www.astro.yale.edu/MUSYC>

SIMPLE catalog, $\gtrsim 60\%$ ²³ of all sources are flagged as blended. This is due to the large PSF of the camera and the depth of the image.

Given the large number of blended sources, it is useful to be able to identify only the most extreme cases of blending. If the sum of the Kron aperture radii of a source and its nearest neighbor exceeds their separating distance and if the neighbor’s flux is brighter than its own, we set the ‘flag_blended’ entry to 4. The percentage of sources suffering from this form of extreme blending is 32% for all sources with $S/N > 5$ at $3.6 \mu\text{m}$.

While performing photometry, we treat blended sources separately. Following Labbé et al (2003) and Wuyts et al. (2008), we use the flux in the color aperture to derive the total flux for sources that suffer from severe blending. For the identification of blended sources, we prefer our own conservative blending criterion over SExtractor’s blending flag, since the latter identifies too many sources as blended, even sources for which the photometry is essentially unaffected²⁴. If we do not make a distinction between blended and non-blended sources, the comparison with other catalogs worsens slightly (< 0.02 mag on the mean deviation).

To determine the color fluxes, we use the circular apertures with $2''$ radius for all sources in all bands:

$$APER(COLOR) = APER(2.0). \quad (1)$$

We calculate the total fluxes from the flux measured in the AUTO aperture. For sources with an aperture diameter smaller than $4''$ diameter, we apply a fixed aperture of $4''$.

$$APER(TOTAL) = \begin{cases} APER(AUTO), & A_{ptot} > 4'' \\ APER(COLOR), & A_{ptot} \leq 4'' \end{cases} \quad (2)$$

Where A_{ptot} is the circularized diameter of the Kron aperture. If the source is blended (FLAG_BLENDED = 4), then

$$APER(TOTAL) = APER(COLOR) \quad (3)$$

Finally, we apply an aperture correction to the total fluxes using the growth curve of bright stars to correct for the minimal flux lost because it fell outside the “total” aperture.

For the IRAC data, we apply individual growth curves for each band. The zeropoint for the aperture correction is based on the values listed in Table 5.7 of the IRAC Data Handbook²⁵. We use the zeropoint in an aperture of $7''.3$ diameter (3 pixel radius in Table 5.7)²⁶. For

²³ Sixty-two percent of the sources suffer from blending (SExtractor’s FLAGS keyword=1), 61% of the sources have a close neighbor (FLAGS = 2), and for 66% of the sources FLAGS=1 \vee FLAGS=2.

²⁴ Adopting the SExtractor blending flag would produce a catalog that mostly consists of blended sources ($\sim 90\%$ for sources with a $5-\sigma$ detection at $4.5 \mu\text{m}$ and in the K -band). These would all be assigned color fluxes that are, in our case, measured within a fixed aperture. The effect such a large fraction of aperture fluxes has on the comparison with the MUSYC catalog can be seen in Fig. 18 of Appendix A. The upper left panel shows a large tail of bright sources that are significantly offset with respect to a one-to-one relation.

²⁵ <http://ssc.spitzer.caltech.edu/irac/dh>

²⁶ We use this aperture instead of the more generally used $12''$

TABLE 4
APERATURE CORRECTIONS^a

band	$4''$ - $7''.3$	$7''.3$ - $12''$	total correction
K	–	–	1.28
$3.6 \mu\text{m}$	1.22	1.112	1.35
$4.5 \mu\text{m}$	1.24	1.113	1.38
$5.8 \mu\text{m}$	1.37	1.125	1.55
$8.0 \mu\text{m}$	1.42	1.218	1.73

NOTE. — $4''$ is our color aperture, $7''.3$ is taken from Table 5.7 from the IRAC Data Handbook (corresponds to 3 pixel radius in that table), and $12''$ is the zeropoint aperture (see Section 3.4). The numbers in the second column are derived from our growth curves, the third column contains the corrections from the Data Handbook, and the total corrections are listed in the last column.

^a Expressed as total flux divided by the flux in APER(COLOR)

the MUSYC optical-IR data, we use the K -band growth curve to correct the total fluxes in all bands. The aperture corrections are listed in Table 4.

5.2.3. The MIPS $24 \mu\text{m}$ Data

The photometry of the MIPS $24 \mu\text{m}$ image is performed in a different way, because of the larger PSF. Here, we use a deblending model to mitigate the effects of confusion. We use the source positions of the IRAC $3.6 \mu\text{m}$ image, which has a smaller PSF, to subtract modeled sources from MIPS sources that show close neighbors, thus cleaning the image. After this procedure we perform aperture photometry in apertures of $6''$ diameter, and correct fluxes to total fluxes using the published values in Table 3.12 of the MIPS Data Handbook.

In principle a similar approach could have been attempted for the IRAC images themselves. Ground-based K -band data and space-based NICMOS imaging have been successfully used to deblend IRAC images (Labbé et al. 2006, Wuyts et al. 2008). However, whereas the resolution of our K -band image is appropriately high, the image is not deep enough for this kind of modeling.

5.3. Background and Limiting Depths

The determination of the limiting depth depends on the noise properties of the images. To analyze those, we place ~ 4000 circular apertures on the registered and convolved images and measure the total flux inside the apertures. Apertures are placed across the field in a random way, excluding all positions associated with sources using the SExtractor segmentation map. We use identical aperture positions for all bands, and repeat the measurements for different aperture sizes. The distribution of empty aperture fluxes can be fitted by a Gaussian, which provides the flux dispersion of the distribution. The RMS depends on aperture size and is larger for larger apertures (see Fig. 8). The left panel shows the distribution of empty aperture fluxes for channel 1 for apertures of sizes $2''$, $3''$, and $4''$. The right panel shows how the RMS increases with aperture size for all IRAC bands.

diameter because of the high density of sources in our field, which would lead to source confusion at large radii. To avoid these complications, we determine the inner part of the growth curve from our data to a $3''.66$ radius, and combine it with the tabulated values from the handbook at larger radii. In this way, we minimize the effect of blending.

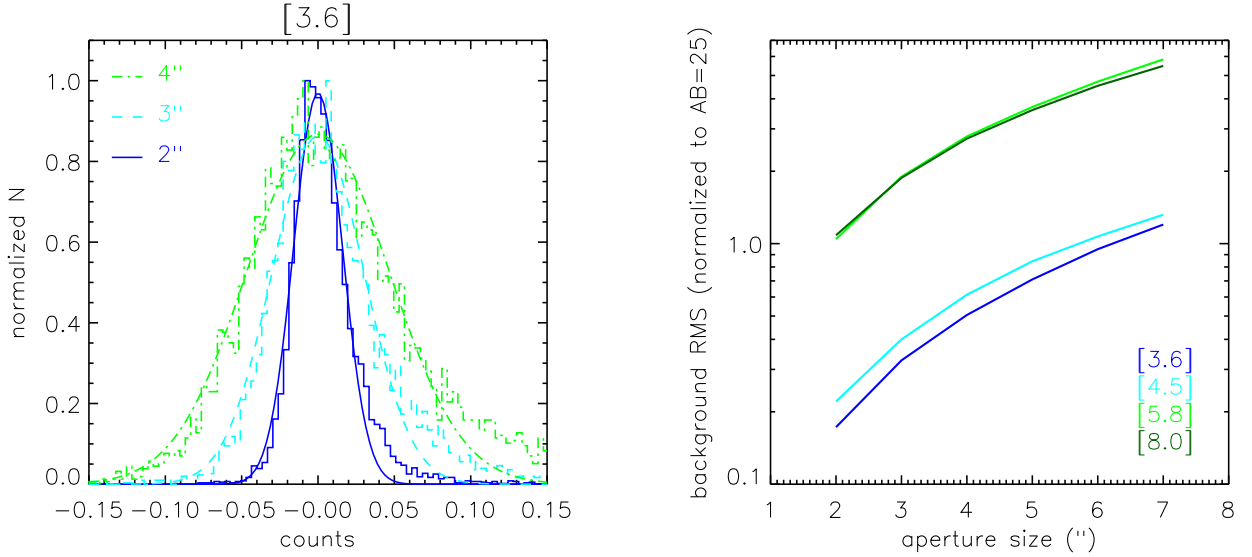


FIG. 8.— Background RMS derived from the distributions of fluxes within randomly placed empty apertures. *Left* - Distribution of empty aperture fluxes within a 2'' (blue), 3'' (cyan), and 4'' (green) aperture diameter on the IRAC 3.6 μm image. The distribution is well described by a Gaussian with an increasing width for increasing aperture size. *Right* - Background RMS as derived from flux measurements within empty apertures versus aperture size for the IRAC bands 3.6 μm (blue), 4.5 μm (cyan), 5.8 μm (green) and 8.0 μm (dark green).

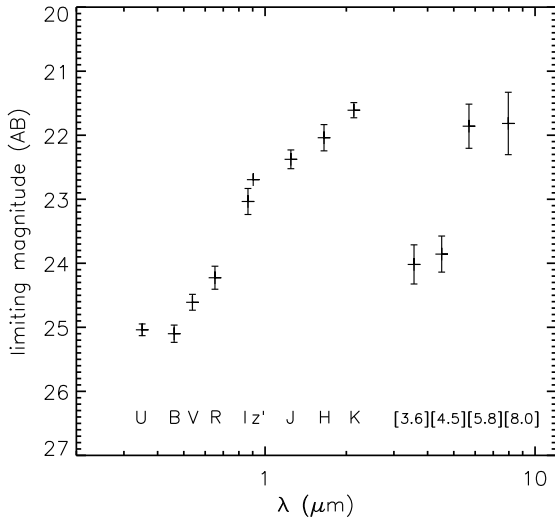


FIG. 9.— Limiting magnitude vs. bandpass wavelength in the SIMPLE catalog. The limiting depths are 5- σ total magnitudes of point sources measured in apertures with a 2''.0 radius. Since the exposure time varies for each band, there is scatter around each limiting magnitude. The error bars denote the standard deviation of this scatter. Since we do not have an exposure map for the z' -band data, there is no error bar at the limiting magnitude of that band (see Taylor et al. 2009b). The IRAC magnitude limits have been determined excluding the GOODS data.

The noise level is higher than can be expected from uncorrelated Gaussian noise. The reason for this is that correlations between neighboring pixels were introduced while performing the data reduction and PSF matching (see also Labbé et al. 2003).

The depth of our SIMPLE IRAC mosaic is a function of position, as some parts have longer exposure times than others. Table 5 lists the total AB magnitude depths at 5- σ for point sources and the area over which this depth is achieved. Figure 9 provides a graphic representation

TABLE 5
5- σ LIMITING DEPTHS (TOTAL AB MAGNITUDE)

percentile	75%	50%	25%	(percentile of pixels)
exptime	>0.9	>1.5	>2.5	(hours)
area	~1200	800	400	(area in arcmin ² with at least this exposure time)
3.6 μm	23.66	23.86	24.00	(depth at 3.6 μm)
4.5 μm	23.50	23.69	23.82	(depth at 4.5 μm)
5.8 μm	21.68	21.95	22.09	(depth at 5.8 μm)
8.0 μm	21.69	21.84	21.98	(depth at 8.0 μm)

of the limiting depths of all wavelength bands.

To investigate whether our measurement of the uncertainties in the IRAC photometry is reasonable, we compare the IRAC fluxes of epoch 1 with those of epoch 2. The results are shown in Fig. 10. The median offsets between the two epochs are printed in the lower left corner and are close to zero in each band. The scatter in each panel is small and comparable to the estimated RMS values.

5.4. Stars

We identify stars by their color and signal to noise ($J - K < 0.04 \wedge wK > 0.5 \wedge (S/N)_K > 5$) and find 978 stars in the total catalog. To test the validity of this selection criterion, we compare it to the BzK selection technique defined by Daddi et al. (2005). In the BzK diagram stars have colors that are clearly separated from the colors of galaxies and they can be identified with the requirement $(z - K) < 0.3 \cdot (B - z) - 0.5$. From the 978 stars in the SIMPLE catalog with sufficient signal to noise in the B - and z -bands, 94% obey the BzK criterion. In the BzK diagram, the remaining 6% lie only slightly above the BzK stellar selection limit.

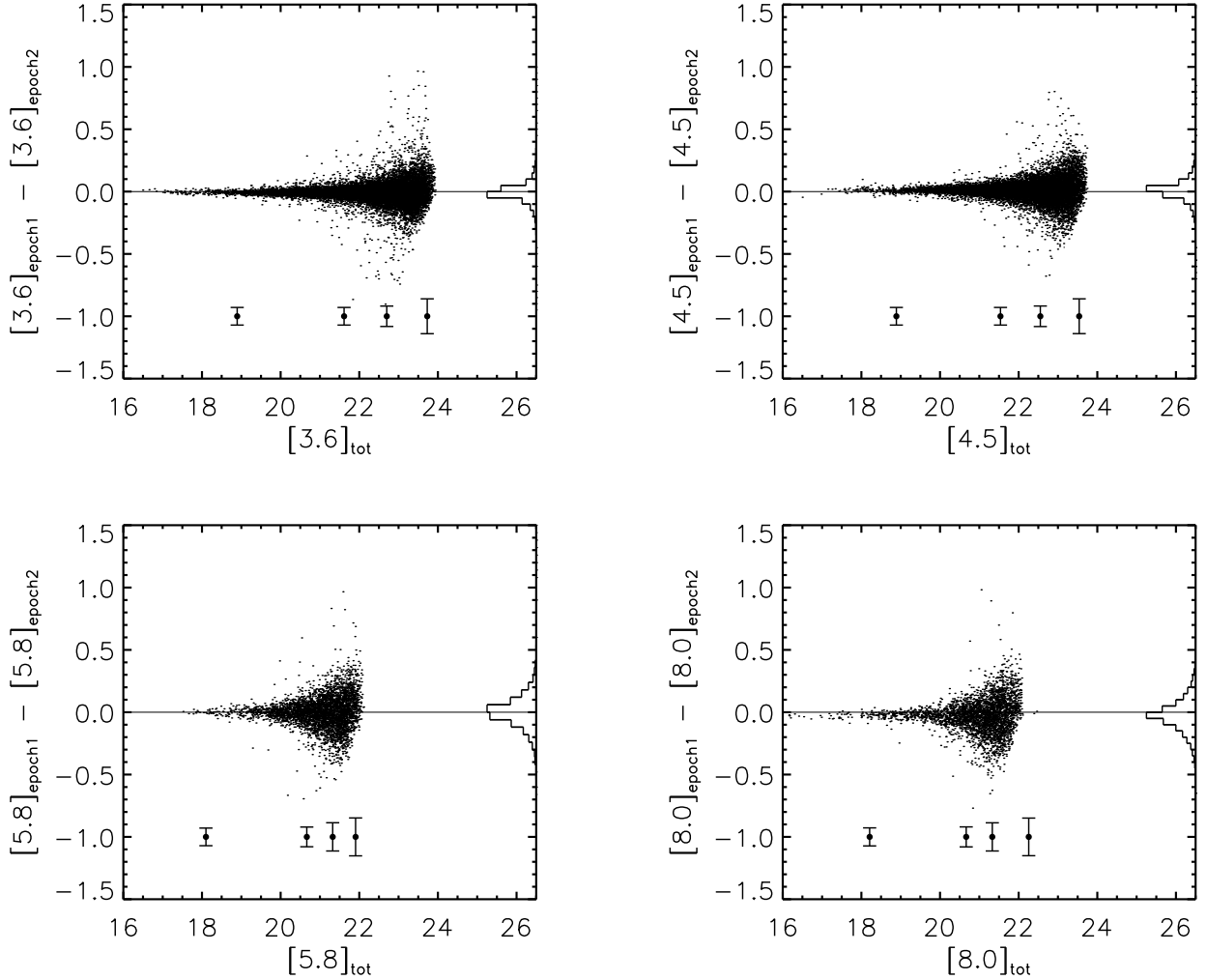


FIG. 10.— Comparison between IRAC magnitudes of the first and second epoch of observations. The panels show the difference between the measured magnitudes of the four IRAC bands. At the right side of each panel, a histogram shows the distribution of the difference. The error bars are the mean errors in bins of equal number of sources, offset by -1 with respect to the measurements.

6. DERIVED PARAMETERS

6.1. Spectroscopic and Photometric Redshifts

The E-CDFS is one of the principal fields for high-redshift studies and has consequently been the object of many spectroscopic surveys. Taylor et al. (2009b) compiled a list of reliable spectroscopic redshifts from several of these surveys, which we cross-correlated with our SIMPLE catalog. The spectroscopic redshifts come from: Croom et al. (2001), Cimatti et al. (2002), le Fèvre et al. (2004), Strolger et al. (2004), Szokoly et al. (2004), van der Wel et al. (2004, 2005), Daddi et al. (2005), Doherty et al. (2005), Mignoli et al. (2005), Ravikumar et al. (2007), Kriek et al. (2008), Vanzella et al. (2008), Popesso et al. (2009), and Treister et al. (2009a). The list contains 2095 spectroscopic redshifts. In addition, we include photometric redshifts from the COMBO-17 survey (Wolf et al. 2004) out to $z=0.7$, which are very reliable at those redshifts. For the remainder of the sources we compute photometric redshifts using the photometric redshift code EAZY (Brammer et al. 2008). The EAZY algorithm provides

a parameter Q_z that indicates whether a derived photometric redshift is reliable. Brammer et al. (2008) show that for $Q_z > 2 - 3$ the difference between photometric and spectroscopic redshifts increases sharply and that quality cuts based on Q_z can reduce the fraction of outliers significantly. Therefore, when testing the accuracy of our photometric redshifts, we only include sources with $Q_z < 2$.

Figure 11 shows the EAZY photometric redshifts compared against a list of spectroscopic redshifts. The upper panel shows the direct comparison for sources with $S/N > 5$ in both K band and $3.6 \mu\text{m}$ (a total of 1280 sources, from which we remove 54 sources with $Q_z \geq 2$ (4%), resulting in a final sample of 1226 sources). The lower panel shows $\Delta z / (1 + z_{\text{spec}})$, where $\Delta z = z_{\text{phot}} - z_{\text{spec}}$. X-ray detections are shown in gray. To quantify the scatter, we determine the normalized median absolute deviation ($\sigma_{\text{NMAD}} = 1.48 \times \text{median} |x - \text{median}(x)|$, which is a robust estimator of the scatter, normalized to give the standard deviation for a Gaussian distribution). Overall the

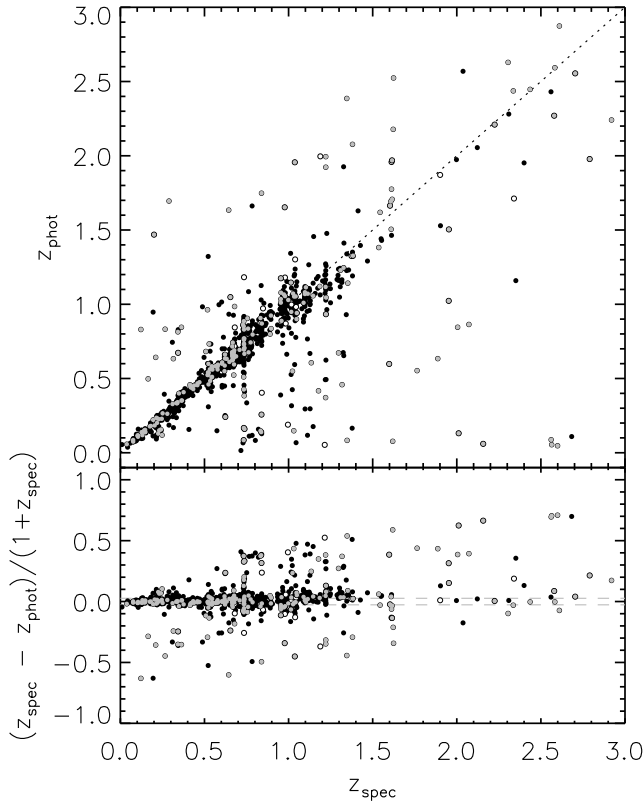


FIG. 11.— Photometric and spectroscopic redshifts in the E-CDFS. *Upper panel* - Direct comparison between photometric and spectroscopic redshifts for 1,226 IRAC detected sources with reliable z_{spec} identification and coverage in all wavelength bands. The dotted line represents a one-to-one relationship. *Lower panel* - Residuals $dz = z_{\text{spec}} - z_{\text{phot}}/(1 + z_{\text{spec}})$ as a function of spectroscopic redshift. The σ_{NMAD} is 0.025, indicated by the dashed lines. Open circles denote AGN candidates, identified by their X-ray flux.

σ_{NMAD} of $|\Delta z|/(1 + z_{\text{spec}})$ is 0.025, but it varies with redshift, ranging from 0.024 at $z \sim 1$, 0.055 at $z \sim 1.5$, and 0.38 at $z \sim 2.0$. There is a significant fraction (8.2%) of outliers with $|\Delta z|/(1 + z_{\text{spec}}) > 5\sigma_{\text{NMAD}}$. This number agrees well with the 11% Taylor et al. (2009b) found for the MUSYC catalog. Many of the outliers are detected in X-ray and are AGN candidates (43%). The high fraction of (candidate) AGN outliers could be explained by the fact that we do not have an AGN spectrum in our template set. EAZY photometric redshifts for X-ray detections are, therefore, uncertain. If we remove them from the sample, the overall accuracy improves and σ_{NMAD} becomes 0.024, 0.041, and 0.16 at redshifts $z \sim 1.0$, 1.5, and 2.0, respectively.

Including AGN templates will improve the overall accuracy of the photometric redshift, as can be seen in Luo et al. (2010). Those authors determine the photometric redshifts of a sample of X-ray sources in the E-CDFS, using UV-to-IR data, including the SIMPLE 3.6 μm -band. Apart from standard galactic templates they used 10 different AGN templates. In the comparison with spectroscopic redshifts, there are only three outliers, which is 1.4% of the sample and the $\sigma_{\text{NMAD}} = 0.010$.

We also check whether the outliers suffer from blending.

Out of the 101 outliers, 26 sources have a neighboring source whose APER(AUTO) exceeds their separating distance and whose flux is at least as bright as its own, which can affect their photometry. However, removing these sources from the sample does not decrease σ_{NMAD} , since there are many sources with nearby bright companions whose photometric and spectroscopic redshifts agree well.

6.2. Star Formation Rates, Rest-frame Photometry and Stellar Masses

In this section, we describe the main characteristics of the procedures for deriving star formation rates and stellar masses. For a more detailed description, the reader is referred to Damen et al. (2009a). We estimated SFRs using the UV and IR emission of the sample galaxies. We use IR template spectral energy distributions (SEDs) of star forming galaxies of Dale & Helou (2002) to translate the observed 24 μm flux to L_{IR} . First, we convert the observed 24 μm flux density to a rest-frame luminosity density at $24/(1 + z)$ μm , then we extrapolate this value to a total IR luminosity using the template SEDs. To convert the UV and IR luminosities to an SFR, we use the calibration from Bell et al. (2005), which is in accordance with Papovich et al. (2006), using a Kroupa IMF:

$$\Psi/M_{\odot} \text{ yr}^{-1} = 1.09 \times 10^{-10} \times (L_{\text{IR}} + 3.3 L_{2800})/L_{\odot}, \quad (4)$$

where $L_{2800} = \nu L_{\nu, (2800\text{\AA})}$ is the luminosity at rest frame 2800 \AA , a rough estimate of the total integrated UV luminosity (1216-3000 \AA).

To obtain stellar masses, we fitted the UV-to-8 μm SEDs of the galaxies using the evolutionary synthesis code developed by Bruzual & Charlot 2003. We assumed solar metallicity, a Salpeter IMF, and a Calzetti reddening law. We used the publicly available HYPERZ stellar population fitting code (Bolzonella et al. 2000) and let it choose from three star formation histories: a single stellar population (SSP) without dust, a constant star formation (CSF) history, and an exponentially declining star formation history with a characteristic timescale of 300 Myr (τ_{300}), the latter two with varying amounts of dust. The derived masses were subsequently converted to a Kroupa IMF by subtracting a factor of 0.2 dex. We calculated rest-frame luminosities and colors by interpolating between observed bands using the best-fit templates as a guide (see Rudnick et al. 2003 and Taylor et al. 2009a for a detailed description of this approach and an IDL implementation of the technique dubbed 'InterRest'²⁷).

7. CATALOG CONTENTS

The SIMPLE IRAC-selected catalog with full photometry and explanation is publicly available on the Web²⁸. We describe the catalog entries below.

²⁷ <http://www.strw.leidenuniv.nl/~ent/InterRest>

²⁸ <http://www.strw.leidenuniv.nl/~damen/SIMPLE.release.html>

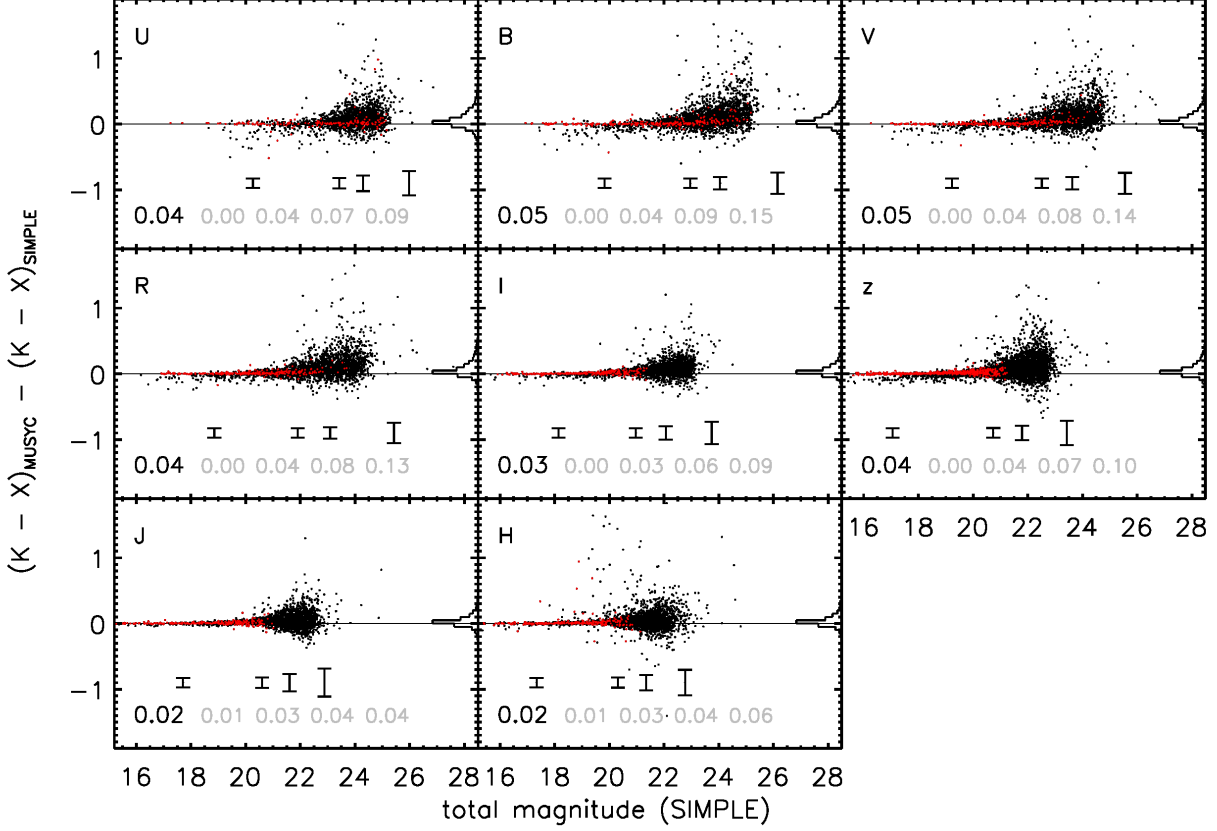


FIG. 12.— Direct comparison between MUSYC and SIMPLE colors in the overlapping bands ($U - K$) for sources with $S/N > 10$ in SIMPLE K -band. At the right side of each panel, a histogram shows the distribution of the offsets. Stars are shown in red. The median offset is indicated at the lower left corner of each panel. For each band only the SIMPLE sources with $S/N > 5$ are included. The error bars indicate the formal errors expected from the SIMPLE and MUSYC photometric errors. They are mean values in bins of equal number of sources and are offset by -1 with respect to the measurements.

- *ID* — A running identification number in catalog order as reported by SExtractor.
- *x_pos, y_pos* — The pixel positions of the objects based on the combined $3.6 \mu\text{m} + 4.5 \mu\text{m}$ detection map.
- *ra, dec* — The right ascension and declination in equinox J2000.0 coordinates, expressed in decimal degrees.
- *i_colf* — Observed color flux in bandpass i , where $i = U, B, V, R, I, z', J, H, K, irac1, irac2, irac3, irac4$ in circular apertures of $4''$ diameter. All fluxes are normalized to an AB magnitude zeropoint of 25.
- *i_colfe* — Uncertainty in color flux in band i (for derivation see Section 5.3).
- *j_totf* — Estimate of the total flux in band j , where $\{j = K, irac1, irac2, irac3, irac4\}$, corrected for missing flux assuming a PSF profile outside the aperture, as described in Section 5.2.1.
- *j_totfe* — Uncertainty in total flux in band j .
- *ap_tot-j* — Aperture diameter (in $''$) used for measuring the total flux in band j . This corresponds the circularized diameter of APER(AUTO) when the Kron aperture is used. If the circularized diameter is smaller than $4''$, the entry is set to APER(COL) = $4''$ (see Section 5.2).
- *iw* — Relative weight for each band i . For the IRAC bands, the weights are determined with respect to the deepest area of the SIMPLE mosaic without GOODS.
- *flag_star* — Set to 1 if the source meets the criteria of Section 5.4.
- *flag_blended* — Contains the SExtractor deblending flag, which indicates whether a source suffers from blending (bit = 1) or whether it has a close neighbor (bit = 2). If a source suffers from extreme blending (see Section 5.2) then bit = 4.
- *flag_qual* — Bitwise added quality flag, that indicates whether a source lies in the GOODS area (bit = 1), lies in a stellar trail (bit = 2), falls outside the MUSYC field (bit = 4) or has been corrected for muxbleed.

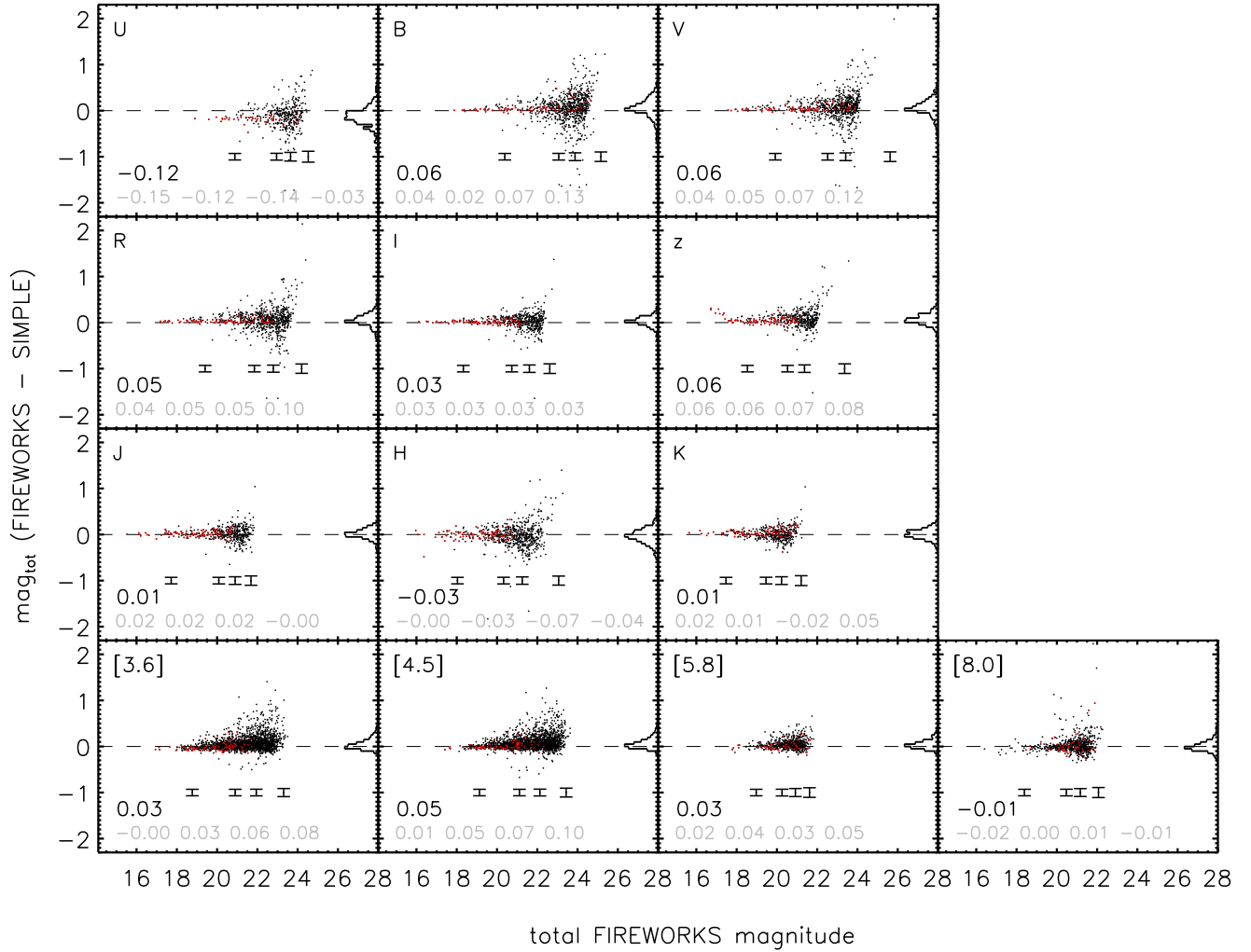


FIG. 13.— Direct comparison of total magnitudes for sources with $S/N > 10$ at $4.5 \mu\text{m}$ for the $U-K$ + IRAC bands of the FIREWORKS catalog and our SIMPLE catalog. At the right side of each panel, a histogram shows the distribution of the offsets. The median offset is indicated at the lower left corner of each panel. For each band only the SIMPLE sources with $S/N > 10$ are included. The error bars indicate the formal errors expected from the SIMPLE and FIREWORKS photometric errors. They are mean values in bins of equal number of sources and are offset by -1.5 with respect to the measurements. All blended FIREWORKS sources have been removed from this figure.

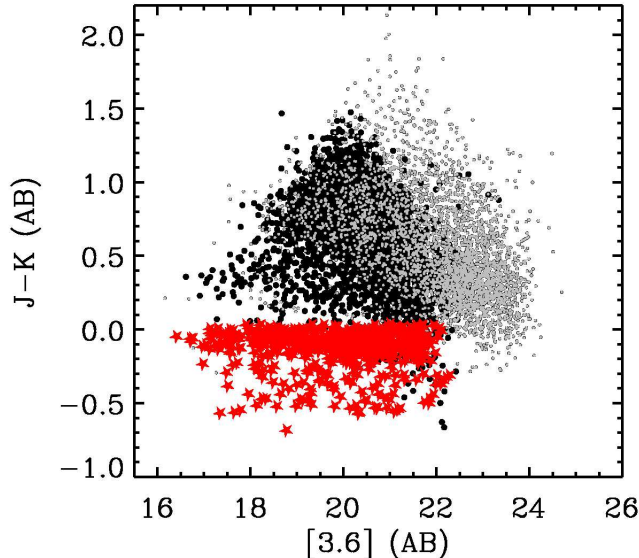


FIG. 14.— $J-K$ vs. $[3.6]$ color-magnitude diagram for IRAC-selected sources in the E-CDFS. Stars (red stars) are identified by their $J-K$ color (see Section 5.4). Overplotted in gray are the values from the FIREWORKS catalog, which reaches greater depth, but contains fewer sources out to a magnitude of 21.5. All blended FIREWORKS sources have been removed from this figure.

Please note that all flux units in the catalog are converted to the same zeropoint on the AB system: $AB_MAG = 25. - 2.5 \log(flux)$.

8. COMPARISON TO OTHER CATALOGS

In this section, we compare our SIMPLE catalog to the published catalogs of Taylor et al. (2009; MUSYC, E-CDFS) and Wuyts et al. (2008; FIREWORKS, CDFS). All catalogs cover (parts of) the same area in the sky. The important difference is that we detect sources in the IRAC $3.6 \mu\text{m}$ and $4.5 \mu\text{m}$ bands, whereas both the MUSYC and the FIREWORKS catalogs are K -band detected. The advantage of an IRAC-selected catalog is that IRAC probes the rest-frame NIR out to high redshift. The downside of IRAC selection is the lower resolution, which leads to confusion. The FIREWORKS catalog used a K -band selection specifically for this reason. We will investigate the effect these differences have on the catalogs below.

8.1. SIMPLE versus MUSYC

The optical-NIR part of the SIMPLE catalog ($U-K$) is based on the same data as the MUSYC catalog. The differences lie in the PSF, detection method, and photometry. Taylor et al. (2009b) determine their total fluxes in a similar way as we do. However, they include an extra correction based on the measurement of the background, which they measure themselves instead of using the value derived by SExtractor and they do not make a distinction between blended and non-blended sources. We cross-correlated the two catalogs and in Fig. 12 we present the comparison. Each panel shows sources with $S/N > 10$ in IRAC $4.5 \mu\text{m}$ and in the relevant band of the panel. We also applied a weight cut in K , $wK > 0.75$, recommended by Taylor et al. (2009b). We determined

the median offsets in different magnitude bins and show them at the bottom of each panel. The first number (in black) represents the median offset of all sources, the gray numbers represent the median offset in each magnitude bin; they are $\lesssim 0.05$ in all bands. The error bars represent the formal expected photometric errors, which are dominated by the Poisson uncertainties in the background. The offsets at bright magnitudes are not caused by Poisson statistics, but most likely by slight systematic differences in methodology. We investigated the bright sources in the U -, B -, V -, and R -band, which show an offset of > 0.2 in color and found that this is an effect of the aperture sizes that were used. The MUSYC fluxes were determined using SExtractor’s `MAG_ISO`, enforcing a minimum aperture diameter of $2''.5$. For the SIMPLE catalog, we used a fixed $4''.0$ aperture diameter. The large color differences at the bright end occur for galaxies for which the differences in aperture size are large too (factor 1.5 and greater).

8.2. SIMPLE versus FIREWORKS

8.2.1. Photometry

The FIREWORKS catalog is constructed from observations in wavelength bands that in some cases differ from the ones we use. The $UBVR$ and I data come from the Wide Field Imager and are the same as we use, except for the U -band, for which the FIREWORKS uses the U_{38} -imaging. The z_{850} -band image was observed by HST, J , H , and K_s data come from ISAAC. The IRAC images were taken by the GOODS team and are nearly the same as the ones we use. Figure 13 shows the comparison of all these bands against each other. As in Fig. 12, we only show sources with $S/N > 10$ in IRAC $4.5 \mu\text{m}$ and in the relevant band of the panel, with a weight in K -band larger than 0.5. The median values are once more shown at the bottom left and the error bars again represent the expected formal errors. The FIREWORKS catalog allows easy identification of blended sources and we have removed these from Fig. 13, since they worsened the comparison. This can be seen in Fig. 19 in Appendix B, which shows the difference in K -band magnitude for FIREWORKS and SIMPLE. In that figure, we did include the blended FIREWORKS sources and marked them in red. They form a specific tail and we have removed them from all further analysis. The sources that suffer from extreme blending in the SIMPLE catalog do not take up such a specific locus in the comparison figures. Excluding them from the sample does not significantly affect the comparison and therefore we keep them in the sample (see Appendix B). In Fig. 13, the comparison between FIREWORKS and SIMPLE tails upward at the faint end. There, the SIMPLE fluxes are brighter than FIREWORKS. This could be due to the fact that the SIMPLE apertures are quite large and will catch some light from neighboring sources.

A direct comparison between SIMPLE and FIREWORKS illustrates the strengths of both data sets as can be seen in Fig. 14, which shows a color-magnitude diagram of both catalogs for sources with $S/N > 5$ in the relevant bands. The envelopes at the bright end agree well, but at the faint end FIREWORKS reaches greater

depth. The advantage of the SIMPLE survey is its large area, and thus its large number of sources. Out to a magnitude of 21.5 in [3.6], the SIMPLE catalog contains 4061 sources at 5- σ , compared to 1,250 for FIREWORKS.

8.2.2. Derived Properties

In addition to a comparison of the photometry, we compare derived quantities of the FIREWORKS and SIMPLE catalogs. Figure 15 shows the comparison between mass, (specific) star formation rate, MIPS 24 μm flux, and redshift. Mean values in bins of equal number of sources are indicated by the red line and given at the bottom of each panel.

The panels with MIPS 24 μm flux and SFR show the best agreement, although the scatter in the comparison of the SFR is substantially higher than it is for the MIPS fluxes. This is caused by the difference in photometric redshifts. If we use FIREWORKS photometric redshifts to determine the SIMPLE SFRs, the scatter in the SFRs is reduced to the scatter in MIPS fluxes.

The scatter is highest in the panels where masses and specific star formation rates (sSFRs) are compared, quantities that depend on photometric redshifts and model assumptions. These are, therefore, more susceptible to systematic errors. Since the masses are derived in similar ways for SIMPLE and FIREWORKS (same models, dust extinction law, metallicity, and IMF), systematics in the modeling can not be responsible in this comparison. We redetermined our masses using FIREWORKS photometric redshifts and found that this reduces the number of outliers in the mass-comparison panel, but not the scatter. The main reason for the scatter in mass and sSFR is signal to noise. The mean absolute deviation of the scatter in the mass comparison is 0.5 for sources with $(\text{S/N})_K < 10$. For sources with a $(\text{S/N})_K \sim 20$, the scatter is reduced to 0.1. Further discussion on the differences between FIREWORKS and SIMPLE fluxes and derived parameters can be found in Appendix C.

9. EVOLUTION OF THE SPECIFIC STAR FORMATION RATE

In a recent paper (Damen et al. 2009a), we showed how the specific star formation rate (SFR per unit mass, sSFR) evolves with redshift. These findings were based on a bright sub-sample of a preliminary version of the SIMPLE catalog, in which total fluxes were crudely determined by applying an aperture correction to the color fluxes. In this section, we briefly revisit the results of Damen et al. (2009a) and show if and how they change, using the final version of the catalog. For details on the derivation of star formation rates and masses, see Damen et al. (2009a).

For this analysis, we created a sub-sample of our catalog out to $z = 1.8$. We selected all sources with $([3.6] + [4.5])/2 < 21.2$, a limit that is chosen so that 95% of the selected sources has an $\text{S/N} > 5$ in the K-band. From this sub-sample, we excluded all stars and all X-ray detections, since they are likely AGNs. The final sample contains 3391 sources. Figure 16 shows how the mean sSFR evolves with redshift in different mass bins, the mean values are also given in Table 6. It

agrees very well with the corresponding figure in Damen et al. (2009a), and all conclusions remain the same. The sSFR increases with redshift for all mass bins and the slope ($d\log(\text{sSFR})/dz$) does not seem to be a strong function of mass (see also Damen et al. (2009b)). To quantify this, we fitted the sSFR with $(1+z)^n$ over the redshift range where we are complete with respect to mass. The value of the slope n is 5.1 ± 0.6 and 4.6 ± 0.3 for galaxies with masses $10.5 < \log(M/M_\odot) \leq 11$ and $\log(M/M_\odot) > 11$, respectively. These numbers are consistent within 1- σ with results based on the FIREWORKS catalog over the same redshift range (3.8 ± 0.8 ($z < 0.8$), and 4.9 ± 0.9 ($z < 1.8$), for both mass bins, respectively; Damen et al. 2009b).

However, the number of galaxies in each bin has changed with the new version of the catalog and this influences the fraction of quiescent galaxies at the highest mass bin. We define a galaxy to be quiescent when its sSFR is smaller than one-third of the inverse of the Hubble time at its redshift ($\text{sSFR}(z) < 1/(3 * t_H(z))$). In Damen et al. (2009a) the fraction of quiescent galaxies decreased with redshift out to $19\% \pm 9\%$ at $z = 1.8$. Figure 17 shows the updated version of this fraction. The old numbers are represented by dashed lines. The slope is less steep and the fraction of quiescent galaxies at $z = 1.8$ is higher, $30\% \pm 7\%$. Although these numbers are consistent within 1- σ , we investigate the cause of this change and find that it can be explained by the increased total fluxes, which change the masses and redshifts. The new value is in better agreement with recent estimates Kriek et al. (2008) ($36\% \pm 9\%$) and I. Labbé et al. (in preparation) ($35\% \pm 7\%$).

We have checked whether these results are robust against blending. We redetermined mean sSFRs for two different samples, removing all sources that (1) were flagged as blended by SExtractor and (2) we consider blended by our own criterion. In the latter case, the mean sSFRs change by less than 5%, in no preferred direction and the fraction of quiescent galaxies does not change. When all sources that were flagged as blended by SExtractor are removed, less than 10% of the sources remain in each mass bin. Whereas the resulting mean sSFRs can differ up to $\sim 40\%$ from the original values, they are scattered around the mean sSFRs that are based on all sources. Hence, the global trends stay remarkably intact and the fact that our sample contains blended sources has no impact on the results.

10. SUMMARY

The *Spitzer* IRAC/MUSYC Public Legacy Survey in the Extended Chandra Deep Field South (SIMPLE) consists of deep IRAC observations (1-1.5 hr per pointing) covering the ~ 1600 arcmin² area surrounding the GOODS CDF-South. This region of the sky has extensive supporting data, with deep observations from the X-rays to the thermal infrared. We describe in detail the reduction of the IRAC observations and the treatment of the main artifacts, such as column pull-down, muxbled, and muxstriping. The final SIMPLE IRAC mosaics were complemented with $10' \times 12'$ GOODS-IRAC images in the center and are available online.

We also present a 13-band, IRAC-detected catalog based on the SIMPLE images and existing public optical

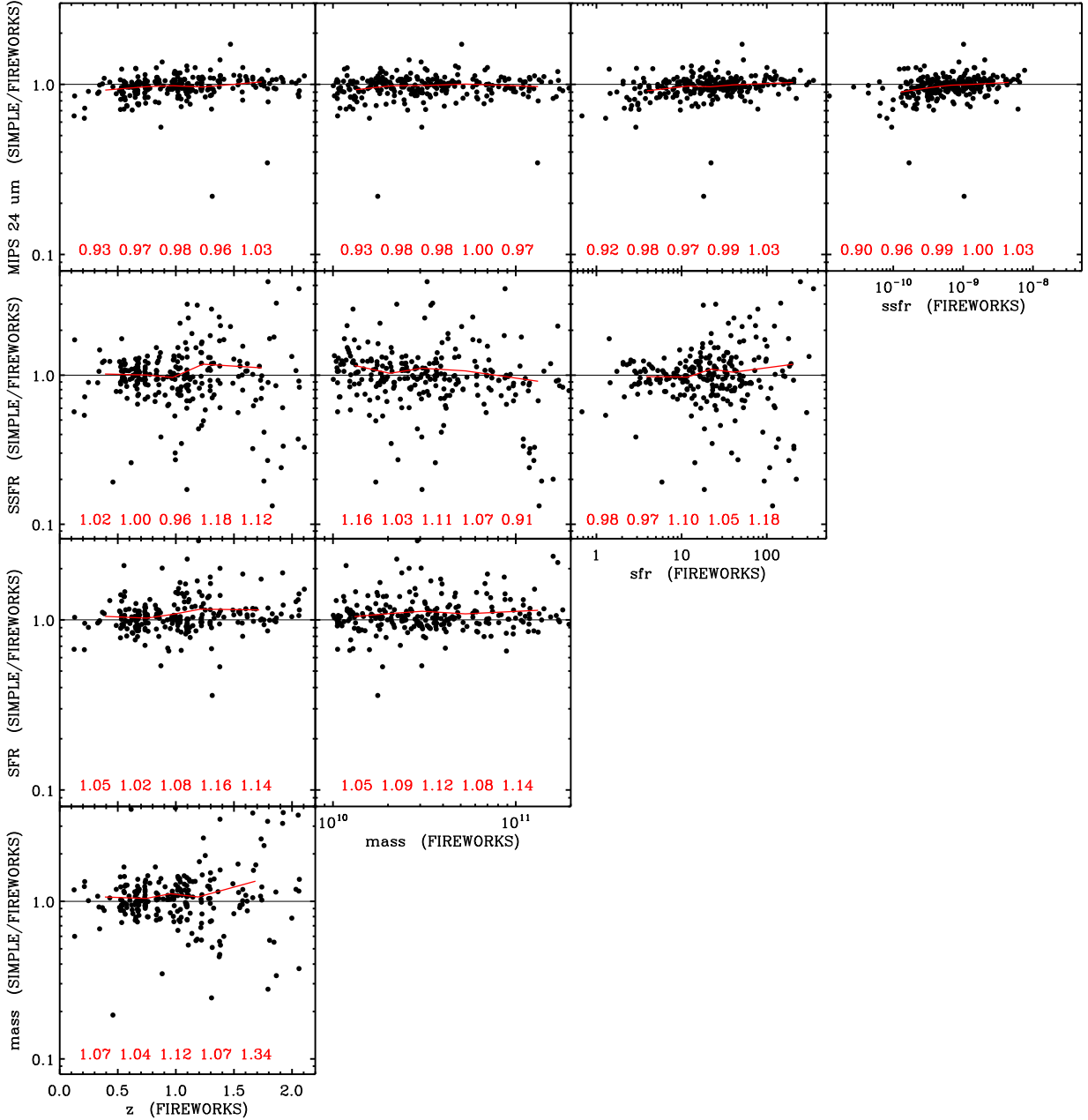


FIG. 15.— Comparison between various observed or derived quantities in FIREWORKS and SIMPLE. The red line indicates a binned mean of the difference in each quantity. The mean values are derived for five intervals of equal number of sources and are shown in red at the bottom of each panel. All blended FIREWORKS sources have been removed from this figure.

and NIR data of the MUSYC project. The wavelength bands that are covered are $UBVRIz'JHK$ and the four IRAC bands at 3.6, 4.5, 5.8, and 8.0 μm . The 5- σ IRAC depths are 23.8, 23.6, 21.9, and 21.7 for [3.6], [4.5], [5.8], and [8.0], respectively. The current catalog is an updated version of the one used in Damen et al. (2009a). We have revisited our results in that work and found that the conclusions stay mainly the same. Investigating the evolution of

the star formation rate we confirmed that the sSFR increases with redshift in all mass bins and that the rate of increase ($d\log(sSFR)/dz$) does not seem to be a strong function of mass. This is in agreement with previous work by Zheng et al. (2007) and Damen et al. (2009b). However, the redshift range over which we have determined the slope of the sSFR is small and differs per mass bin due to incompleteness at the low-mass end. We can

TABLE 6
SPECIFIC STAR FORMATION RATES IN MASS AND REDSHIFT BINS

z	sSFR (10^{-9} yr^{-1})		
	$10 < \log(M_*/M_\odot) < 10.5$	$10.5 < \log(M_*/M_\odot) < 11$	$\log(M_*/M_\odot) > 11$
0.2	0.11 ± 0.02	0.053 ± 0.015	---
0.4	0.23 ± 0.02	0.081 ± 0.016	0.025 ± 0.009
0.6	---	0.19 ± 0.02	0.046 ± 0.007
0.8	---	0.27 ± 0.02	0.067 ± 0.016
1.0	---	---	0.12 ± 0.02
1.2	---	---	0.13 ± 0.02
1.4	---	---	0.35 ± 0.05
1.6	---	---	0.42 ± 0.05
1.8	---	---	0.58 ± 0.10

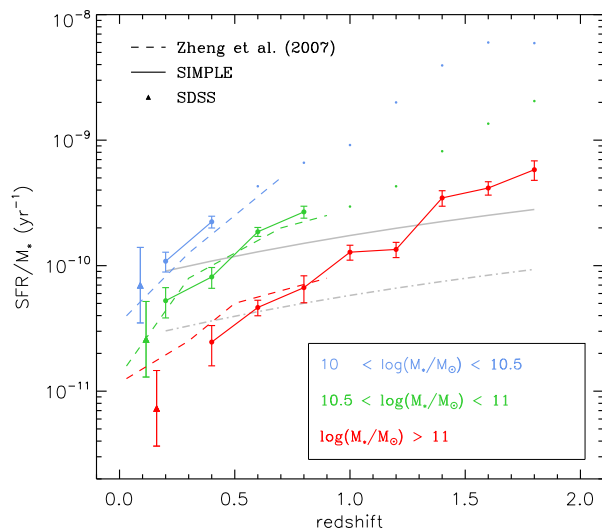


FIG. 16.— Specific star formation rate versus redshift. This figure is an updated version of Figure 3 of Damen et al. (2009a), based on improved total fluxes. Filled circles are SIMPLE results, dots show where we become incomplete with respect to mass. Triangles denote SDSS data. The error bars represent bootstrap errors for SIMPLE and a systematic error of 0.3 dex for the SDSS data. The dashed colored lines represent the results from Zheng et al. (2007) in identical mass bins. The gray solid line is the inverse of the Hubble time ($1/t_H$ in yr^{-1}). Sources above this line are in starburst mode. The time it would take to produce the current stellar mass at the current SFR is smaller than a Hubble time. Star formation is quenched in galaxies under the gray dashed line ($1/(3 \times t_H)$); the bulk of their stars has already been formed. The sSFR increases with z at a rate that appears independent of mass and sSFRs of more massive galaxies are typically lower than those of less massive galaxies over the whole redshift range.

use the deeper FIREWORKS catalog to investigate the possible (lack of) evolution of n with mass out to higher redshift ($z = 1.5$) in the three mass bins of Fig. 16. The values for the FIREWORKS n are consistent with the SIMPLE n within $1-\sigma$, although the number statistics in the highest mass bin are low (on average eight sources per redshift bin). We can conclude that the logarithmic increase of the sSFR with redshift is at least not a strong function of mass.

We investigated the fraction of massive galaxies that show suppressed star formation and found that at $z \sim 1.8$, $30\% \pm 7\%$ of the massive galaxies ($M_* > 10^{11}$

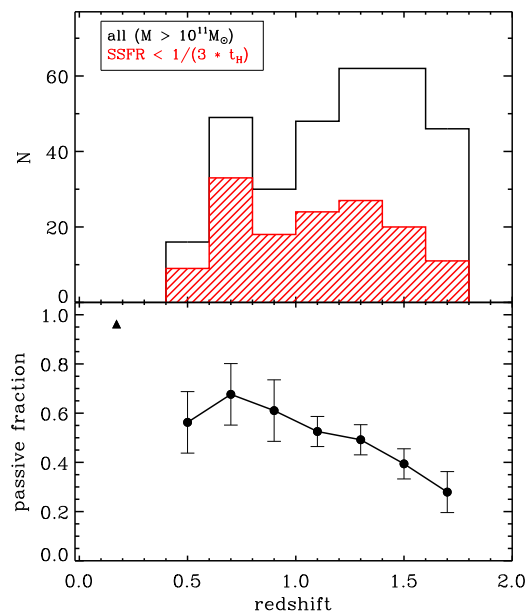


FIG. 17.— The redshift evolution of the fraction of quiescent galaxies with $M_* > 10^{11} M_\odot$. This figure is an updated version of Figure 6 of Damen et al. (2009a), based on improved total fluxes. The numbers are consistent with each other within $1-\sigma$. Quiescent galaxies are defined as sources with $s\text{SFR} < 1/(3 \times t_H)$ yr^{-1} , where t_H is the age of the universe at the source's redshift. The upper panel shows the distribution of all redshift in this mass range, overlaid is the number of galaxies whose star formation is quenched. The lower panel shows the fraction of galaxies in quiescent mode. The error bars represent bootstrap errors. SDSS data have been used to determine a local values (triangle).

M_\odot) have $s\text{SFR} < 1/(3t_H)$, which is our criterion for quenched star formation. This is consistent within $1-\sigma$ with the $19\% \pm 9\%$ from Damen et al. (2009a) and is in better agreement with values from Kriek et al. (2008) and I. Labbé et al. (in preparation), which are $36\% \pm 9\%$ and $35\% \pm 7\%$, respectively.

We thank the referee for the detailed comments that helped us improve the paper significantly. We also thank Leonidas Moustakas for useful discussion and help with the removal of artifacts from the SIMPLE data. This research was supported by grants from the Nether-

lands Foundation for Research (NWO), and the Leids Kerkhoven-Bosscha Fonds. Support from National Science Foundation grant NSF CAREER AST-0449678 is

gratefully acknowledged.
Facilities: Spitzer (IRAC, MIPS)

APPENDIX

A. FLUX APERTURES

When performing photometry we use SExtractor’s AUTO aperture since it is more robust than for instance the ISOCOR aperture, which depends more sensitively on the depth of the image. In addition, it allows an easy comparison with other catalogs such as the MUSYC and FIREWORKS catalogs, which are both based on AUTO apertures. In Fig. 18, we show the effect different apertures have on the comparison between our catalog and the MUSYC catalog. As expected, the AUTO fluxes give the best agreement. The cause of the offset at the bright end of the panel showing the AUTO fluxes is discussed in Section 8.1.

B. CONFUSION

While building the SIMPLE catalog, we treated blended (or confused) sources very conservatively and only identified the sources that most severely suffered from blending. We were not able to simply use the quality flags SExtractor provided, since those identified 60% of all sources as blended. Performing photometry on these “blended” sources in a way commonly used for blended sources, exacerbated the disagreement with other catalogs (see Section 5.2). In addition, it was not possible to model blended sources using a deep source map at lower wavelength, since our K -band data were not deep enough (see Section 5.2.3). The effect blending has on photometry is clear in, e.g., the FIREWORKS catalog, where blended sources were identified by their SExtractor flags and take up 12% of the sample. Figure 19 shows the comparison between the total K -band magnitude of SIMPLE and FIREWORKS. Blended sources in the FIREWORKS catalog are shown in red and form a distinct plume of scattered sources. Since the plume contains only blended sources, we removed these sources from all further analysis, since their photometry must be inaccurate (i.e., Figures 13-15). Unfortunately, we could not apply this trick to the SIMPLE catalog. In Section 5, we identified the sources that suffer from severe blending. We have not indicated them in Fig. 19, since they do not fill a specific locus, but instead are spread out evenly over the whole figure. It is, therefore, not possible to quantify the effect blended sources have on our photometry and derived parameters.

C. SCATTER BETWEEN FIREWORKS AND SIMPLE

In the comparison of the photometric and derived properties of the SIMPLE and FIREWORKS catalogs, we observed a large scatter. In Fig. 20, we show the comparison between MIPS fluxes. The mean values of the difference are indicated by the red line and are printed in red in the lower right corner. Error bars represent the standard deviation in each bin and are printed in red in the lower right corner. The FIREWORKS MIPS fluxes have been determined based on a K -band image with high spatial resolution. On the other hand, the SIMPLE fluxes were determined using our IRAC imaging as a reference (see Section 5.2.3). The IRAC data are deep, but have a PSF which is much larger, leading to more confusion. This causes the difference in MIPS fluxes, which are relatively modest (mean absolute deviation of 10% at the bright end).

In Section 8.2.2, we stated that the scatter in mass was not caused by photometric redshift errors. This can be inferred from Fig. 21, which shows the difference in masses from FIREWORKS and SIMPLE against spectroscopic (*left*) and photometric (*right*) redshift. Despite the disappearance of a few dramatic outliers, it is not clear that the scatter is much reduced when using spectroscopic redshifts only.

REFERENCES

- Alexander, D., et al. 2008, *AJ*, 135, 1968
 Arnouts, S., et al. 2001, *A&A*, 379, 740
 Ashby, L. N., et al. 2009, *ApJ*, 701, 428
 Barger, A. J., Cowie, L. L., Smail, I., Ivison, R. J., Blain, A. W., Kneib, J.-P. 1999, *AJ*, 117, 2656
 Bell, E. F., et al., 2005, *ApJ*, 625, 23
 Bertin, E. & Arnouts, S. 1996, *A&AS*, 117, 393
 Bolzonella, M., Miralles, J.-M., Pellø, R. 2000, *A&A*, 363, 476
 Brammer, G. B., van Dokkum, P. G., Coppi, P. 2008, *ApJ*, 686, 1503
 Bruzual, G., & Charlot, S. 2003, *MNRAS*, 2, 344, 1000
 Cardamone, C. N., et al. 2008, *ApJ*, 680, 130
 Cimatti, A., et al. 2002, *A&A*, 392, 395
 Cimatti, A., et al. 2004, *Nature*, 430, 184
 Cohen, M., Megeath, S. T., Hammersley, P. L., Martín-Luis, F., Stauffer, J. 2003, *AJ*125, 2645
 Croom, S. M., Smith, R. J., Boyle, B. J., Shanks, T., Loaring, N. S., Miller, L., Lewis, I. J. 2001, *MNRAS*, 322, 29
 Daddi, E., Cimatti, A., Pozzetti, L., Hoekstra, H., Röttgering, H. J. A., Renzini, A., Zamorani, G., Mannucci, F. 2000, *A&A*, 361, 535
 Daddi, E., et al. 2005, *ApJ*, 626, 680
 Daddi, E., et al. 2007, *ApJ*, 670, 173
 Dale, D. A. & Helou, G. 2002, *ApJ*, 576, 159
 Damen, M., Labbé, I., Franx, M., van Dokkum, P. G., Taylor, E. N., Gawiser, E. J. 2009a, *ApJ*, 690, 937
 Damen, M., Förster Schreiber, N. M., Franx, M., Labbé, I., Toft, S., van Dokkum, P. G., Wuyts, S. 2009b, *ApJ*, 705, 617
 Dickinson, M., et al. in *The Mass of Galaxies at Low and High Redshift: Proc. of the European Southern Observatory and Universitäts-Sternwarte München Workshop, ESO Astrophysics Symposia, Venice, Italy, 2001 October 24-26*, ed. R. Bender & A. Renzini (Berlin: Springer), 324
 Doherty, M., Bunker, A. J., Ellis, R. S., McCarthy, P. J. 2005, *MNRAS*, 361, 525
 Donley, J. L., Rieke, G. H., Pérez-González, P. G., Barro, G. 2008, *ApJ*, 687, 111
 Elston, R., Rieke, G. H., & Rieke, M. J. 1988, *ApJ*, 331, 77
 Erben T., et al. 2005, *Astron. Nachr.*, 326, 432
 Fazio, G. G., et al. 2004, *ApJS*, 154, 10
 Franx, M. et al. 2003, *ApJ*, 587, 79
 Gawiser, E., et al. 2006, *ApJS*, 162, 1
 Giacconi, R., et al. 2002 *ApJS*, 139, 369
 Giavalisco, M., & The GOODS Team 2004, *ApJ*, 600, L93
 Hildebrandt, H., et al. 2006, *A&A*, 452, 1121
 Kriek, M., et al. 2008, *ApJ*, 677, 219

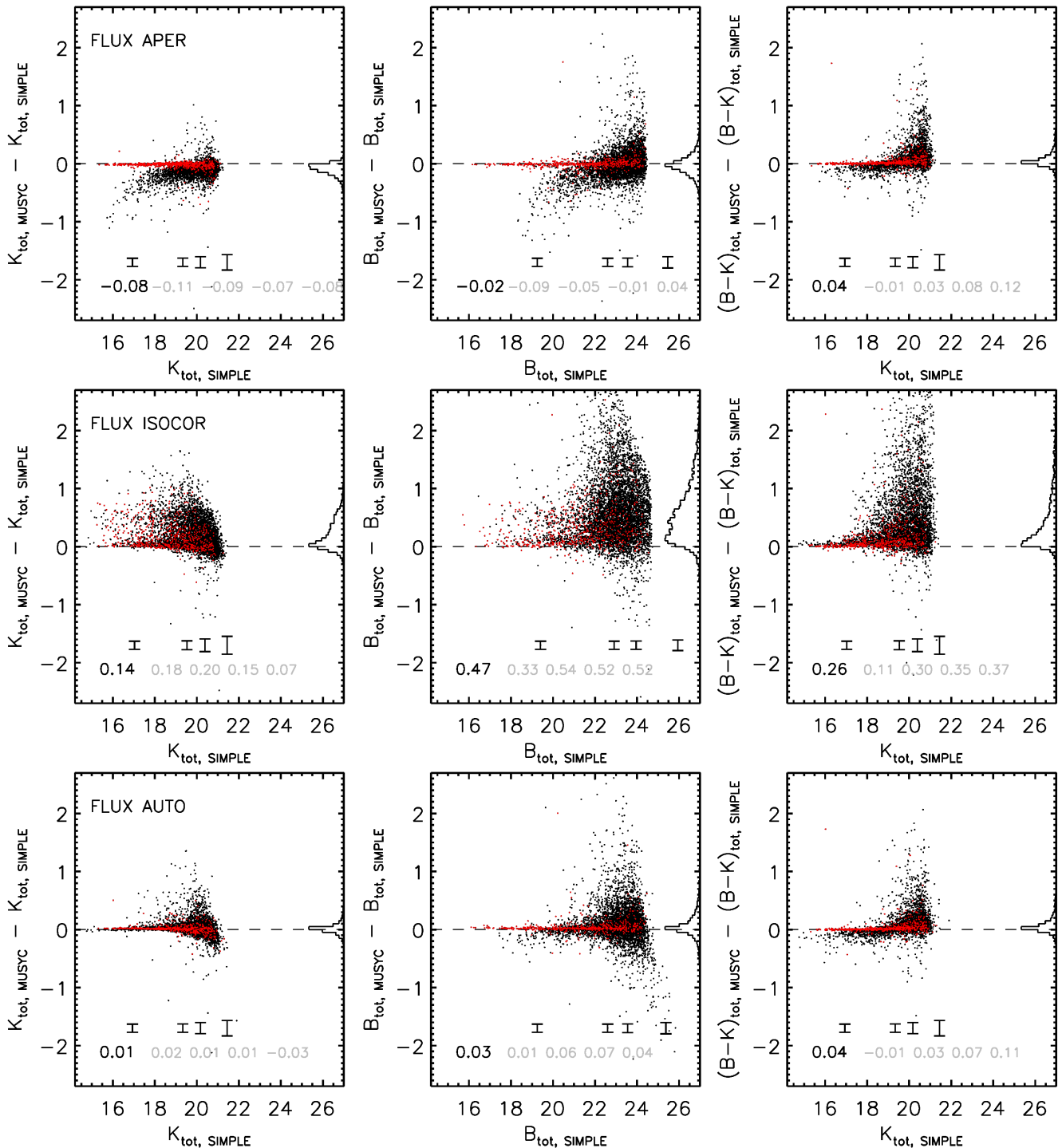


FIG. 18.— Comparison between MUSYC and SIMPLE magnitudes in the B - and K -bands for different apertures. The apertures used are (from top to bottom row) fixed apertures of $4''$ (FLUX APER), corrected isophotal apertures (FLUX ISOCOR), and flexible elliptical apertures (FLUX AUTO). Stars are shown in red. The median offset is indicated at the lower left corner of each panel. For each band only the SIMPLE sources with $S/N > 5$ are included. The error bars indicate the formal errors expected from the SIMPLE and MUSYC photometric errors. They are mean values in bins of equal number of sources and are offset by -1 with respect to the measurements. In the construction of this figure no distinction has been made between blended and non-blended sources.

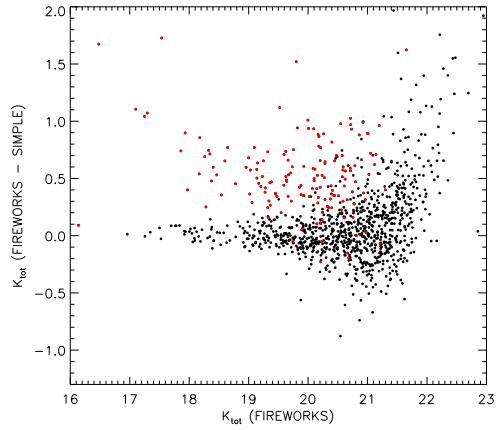


FIG. 19.— Comparison between FIREWORKS and SIMPLE for K -band total magnitude. Sources that are blended in the FIREWORKS catalog are shown in red. We removed these sources from all analysis (i.e., Figures 13-15). The sources that are flagged as blended by SExtractor take up $\geq 60\%$ of the complete SIMPLE sample and even a higher fraction (98%) of the sources shown above, which are relatively bright ($(S/N)_K > 5$).

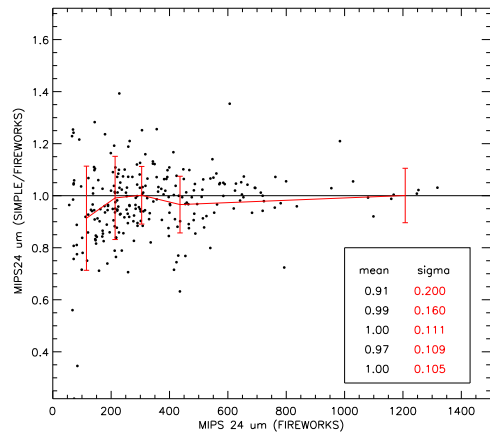


FIG. 20.— Comparison between FIREWORKS and SIMPLE for MIPS 24 μm total magnitude. The mean values are indicated by the red line and printed in the lower right corner, together with the standard deviation in each bin. The formal errors obtained from our deblending routine are smaller than the observed standard deviation. It is clear, however, that the MIPS 24 μm fluxes are consistent with each other within 10%-20%.

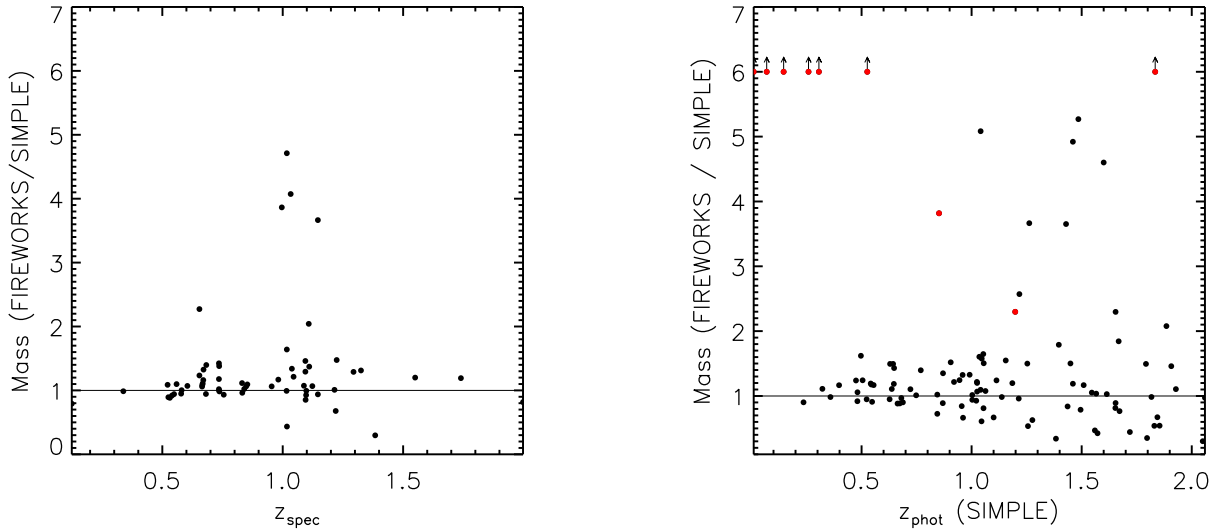


FIG. 21.— Comparison between the masses of FIREWORKS and SIMPLE versus (a) spectroscopic and (b) photometric redshifts. The red points in the right panel represent sources with photometric redshifts that differ more than 0.5 between FIREWORKS and SIMPLE. Despite these outliers, it is clear that the observed scatter is not caused by photometric redshift errors.

- Kroupa, P. 2001, *MNRAS*, 322, 231
 Labbé, I. et al. 2003, *AJ*, 125, 1107
 Labbé, I., Bouwens, R., Illingworth, G. D., Franx, M. 2006, *ApJ*, 649, 67
 Lacy, M., Canalizo, G., Rawlings, S., Sajina, A., Storrie-Lombardi, L., Armus, L., Marleau, F. R., Muzzin, A. 2005, *Mem. Soc. Astron. Ital.*, 76, 154
 ai, K., et al. 2008, *ApJ*, 674, 70
 Lehmer et al. 2005, *ApJS*, 161, 21
 le Fèvre, O., et al. 2004, *A&A*, 428, 1043
 Lonsdale, C. J. et al. 2003, *PASP*, 115, 897
 Luo, B., et al. 2008, *ApJS*, 179, 19
 Luo, B., et al. 2010, *ApJS*, 187, 560
 Magnelli, B., Elbaz, D., Chary, R. R., Dickinson, M., Le Borgne, D., Frayer, D. T., Willmer, C. N. A. 2009, *A&A*, 496, 57
 Martin, D. C., et al. 2005, *ApJ*, 619, 1
 Mignoli, M., et al. 2005, *A&A*, 437, 883
 Miller, N. A., Formalont, E. B., Kellermann, K. I., Mainieri, V., Norman, C., Padovani, P., Rosati, P., Tozzi, P. 2008, *ApJS*, 179, 114
 McCarthy, P. J., et al. 2001, *ApJ*, 560, 131
 Monet, D. G. et al. 2003, *AJ*, 125, 984
 Papovich, C., et al. 2006, *ApJ*, 640, 92
 Popesso, P., et al. 2009, *A&A*, 494, 443
 Quadri, R., et al. 2007, *AJ*, 134, 1103
 Ravikumar, C. et al. 2007, *A&A*, 465, 1099
 Reach, W. T., et al. 2005, *PASP*, 117, 978
 Rix, H.-W., et al. 2004, *ApJS*, 152, 163
 Rudnick, G., et al. 2003, *ApJ*, 599, 847
 Sanders, D. B., et al. 2007, *ApJS*, 172, 86
 Spinrad, H., Dey, A., Stern, D., Dunlop, J., Peacock, J., Jimenez, R., Windhorst, R. 1997, *ApJ*, 484, 581
 Steidel, C. C., Giavalisco, M., Dickinson, M., Adelberger, K. L. 1996, *AJ*, 112, 352
 Steidel, C. C., Adelberger, K. L., Giavalisco, M., Dickinson, M., Pettini, M. 1999, *ApJ*, 519, 1
 Stern, D., et al. 2005, *ApJ*, 631, 163
 Strolger, L.-G., 2004, *ApJ*, 613, 200
 Szokoly, G. P., et al. 2004, *ApJS*, 155, 271 bibitem[Taylor et al. (2009)]
 Taylor, E. N., et al. 2009a, *ApJ*, 694, 1171
 Taylor, E. N., et al. 2009b, *ApJS*, 183, 295
 Treister, E., et al. 2009a, *ApJ*, 693, 1713
 Treister, E., et al. 2009b, *ApJ*, 706, 535
 Vanzella, E., et al. 2008, *A&A*, 478, 83
 van der Wel, A., Franx, M., van Dokkum, P. G., Rix, H.-W., Illingworth, G. D., Rosati, P. 2005, *ApJ*, 631, 145
 van der Wel, A., Franx, M., van Dokkum, P. G., Rix, H.-W. 2004, *ApJ*, 601, 5
 van Dokkum, P. G., et al. 2006 *ApJ*, 638, 59
 Wolf, C., et al. 2004, *A&A*, 421, 913
 Wuyts, S., Labbé, I., Förster-Schreiber, N. M., Franx, M., Rudnick, G., Brammer, G. B., van Dokkum, P. G. 2008, *ApJ*, 682, 985
 Zheng, X. Z., Bell, E. F., Papovich, C., Wolf, C., Meisenheimer, K., Rix, H.-W., Rieke, G. H., Somerville, R. 2007, *ApJ*, 661, 41

